Induced Fit and the Catalytic Mechanism of Isocitrate Dehydrogenase

Susana Gonçalves,[†] Stephen P. Miller,[‡] Maria A. Carrondo,[†] Anthony M. Dean,*[,‡] and Pedro M. Matias*[,†]

[†]Instituto de Tecnologia Química e Biológica, Universidade Nova de Lisboa, Apartado 127, 2780 Oeiras Portugal
[‡]Biotechnology Institute, University of Minnesota, 1479 Gortner Avenue, Saint Paul, Minnesota 55108, United States

S *Supporting Information*

ABSTRACT: NADP⁺ dependent isocitrate dehydrogenase (IDH; EC 1.1.1.42) belongs to a large family of α-hydroxyacid oxidative β-decarboxylases that catalyze similar three-step reactions, with dehydrogenation to an oxaloacid intermediate preceding β-decarboxylation to an enol intermediate followed by tautomerization to the final α-ketone product. A comprehensive view of the induced fit needed for catalysis is revealed on comparing the first "fully closed" crystal structures

of a *pseudo*-Michaelis complex of wild-type *Escherichia coli* IDH (*Eco*IDH) and the "fully closed" reaction product complex of the K100M mutant with previously obtained "quasi-closed" and "open" conformations. Conserved catalytic residues, binding the nicotinamide ring of NADP⁺ and the metal-bound substrate, move as rigid bodies during domain closure by a hinge motion that spans the central β-sheet in each monomer. Interactions established between Thr105 and Ser113, which flank the "phosphorylation loop", and the nicotinamide mononucleotide moiety of NADP⁺ establish productive coenzyme binding. Electrostatic interactions of a Lys100-Leu103-Asn115-Glu336 tetrad play a pivotal role in assembling a catalytically competent active site. As predicted, Lys230* is positioned to deprotonate/reprotonate the α-hydroxyl in both reaction steps and Tyr160 moves into position to protonate C3 following β-decarboxylation. A proton relay from the catalytic triad Tyr160-Asp307-Lys230* connects the α-hydroxyl of isocitrate to the bulk solvent to complete the picture of the catalytic mechanism.
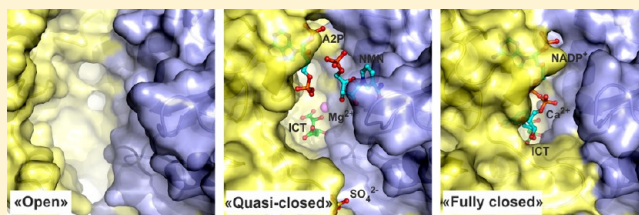
Escherichia coli isocitrate dehydrogenase [IDH; 2R,3S-isocitrate:NADP⁺ oxidoreductase (decarboxylating); EC 1.1.1.42] belongs to a large superfamily of decarboxylating dehydrogenases evolutionarily unrelated to all other enzymes.[1] Each family member uses a three-step mechanism to sequentially catalyze a dehydrogenation at the C2 and a decarboxylation at the C3 of the 2R-malate core common to all substrates, with tautomerization of the enol intermediate to produce the ketone product, viz:
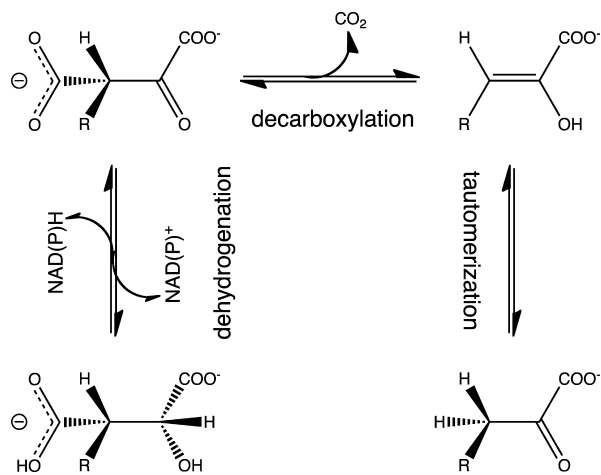
The substrates differ at the 4 position: isocitrate (4 = $-CH_2COO^-$) is an intermediate in Krebs' cycle, isopropylma-

late (4 = $-CH(CH_3)_2$) is an intermediate in leucine biosynthesis, homoisocitrate (4 = $-CH_2CH_2COO^-$) is an intermediate in the α-aminoadipate pathway for lysine biosynthesis in fungi [2] and tartrate (4 = $-OH$) is catabolized by *Pseudomonas putida* and *Agrobacterium vitis*.[3,4] Superpositioned active sites reveal that functional residues interacting with the 2R-malate core are invariant, even among highly divergent family members.[5]

Classic work on IDH catalysis[6−12] established that hydride transfer from C2 to the *re* face of the nicotinamide C4 precedes facile decarboxylation at C3 of the oxaloacid intermediate. Recent work determined that decarboxylation produces an enol intermediate that tautomerizes to the final ketone product.[5] All known IDHs require a divalent metal cation, such as Mg^{2+}, for catalysis. Structural studies of IDH confirm the expected bidentate chelation of Mg^{2+} by the C1 carboxylate and C2 hydroxyl of the substrate needed to stabilize the negative charges formed on the hydroxyl oxygen during the transition states of both steps.[6,13] IDH ternary complex structures also confirm that hydride transfer is to the *re* face of the nicotinamide C4.[14−16]

Less certain are the identities of the catalytic base, needed to initiate dehydrogenation by abstracting the proton from the

isocitrate C2 hydroxyl, and of the catalytic acid, needed to protonate C3 following decarboxylation. The original suggestion[13,17] that Asp283* acts as the base, always dubious given that chelation to Mg^{2+} should reduce its pK_a far below that required for function under physiological conditions, failed to receive support upon detailed investigation.[18] A structurally conserved water has also been proposed as the catalytic base,[19,20] with a proton relay system exiting the active site to allow exchange with bulk solvent. However, no mechanism to reduce the water's pK_a to within a plausibly physiological range was proposed. Replacing the active site Tyr160 by phenylalanine compromised overall activity with isocitrate; decarboxylation of oxalosuccinate was unaffected while its reduction to isocitrate was severely lowered.[21] These results suggested a role for Tyr160 in dehydrogenation, although in all binary complexes of IDHs[19,22–25] and IMDH,[26] and in the ternary complexes of IDH[20,23,27–32] and TDH,[33] the tyrosine side chain is in no position to abstract the proton from the isocitrate C2 hydroxyl. Based on its geometry and spatial proximity to isocitrate in a binary complex, Lys230* was proposed to be the proton donor following decarboxylation.[13] Support for this conjecture was obtained upon replacing Lys230* by methionine which greatly compromised overall activity; decarboxylation of oxalosuccinate was obliterated while its reduction to isocitrate was barely affected.[21] By contrast, detailed kinetic studies of mutations at the equivalent sites in pig heart IDH (Tyr140 and Lys212*) suggest Tyr160 is the acid that protonates the substrate after decarboxylation, with Lys230* playing a supporting role.[34] Recent work on homoisocitrate dehydrogenase[5] has proposed that Lys199* and Tyr126 (equivalent to Lys230* and Tyr160 in EcoIDH) work as a pair, with Lys199* abstracting the proton directly from the C2 hydroxyl during dehydrogenation to the oxaloacid, then reprotonating the hydroxyl during C3 decarboxylation to the enol, and then once again abstracting the proton as Tyr126 protonates C3 to the ketone product.

The confusion surrounding the identities and exact roles of the active site residues is partly attributable to the absence of crystal structures detailing the active site during catalysis. A particular difficulty with EcoIDH (and by inference, other family members too) is that it undergoes substantial conformational changes upon substrate binding, not to the productive Michaelis complex, but rather to an intermediate nonproductive position. Structural data, though informative, may be misleading. Kinetic data from site directed mutants may also mislead when other active site residues partially compensate for loss of a functional group. Here, we determine the structures of several new ternary complexes of wildtype EcoIDH and a catalytically compromised mutant K100M[35] to better resolve the conformational changes needed to produce a productive Michaelis complex and reconcile conflicting hypotheses regarding the catalytic mechanism.

■ MATERIALS AND METHODS

Protein Production and Purification. *E. coli* strain STΔicd[35] was transformed with plasmid (pIDH[wildtype] or pIDH[K100M] containing *E. coli icd* wildtype and Lys100Met mutant genes respectively) and grown at 37° to full density in 5 L of broth (12 g of tryptone, 24 g of yeast extract, 4 g of glycerol, 17 mM KH_2PO_4, 72 mM K_2HPO_4 and 5 mg/L tetracycline) in a 6 L NBS BioFlow 3000 fermentor (University of Minnesota Biotechnology Resource Center). Cells were

harvested by centrifugation and the paste flash frozen between blocks of dry ice and stored at $-80°$ until needed.

Fifty grams of cell paste were resuspended in 150 mL of extract buffer (10 mM KH_2PO_4, 0.5 M NaCl, 2 mM $MgCl_2$, and 2-mercaptoethanol, pH 7.7) and stirred for 1 h at room temperature to allow IDH to become fully dephosphorylated. The suspension was then chilled to 4 °C, sonicated and the cell debris removed by centrifugation. Enzymes were purified by a standard protocol [36] involving ammonium sulfate precipitation, DEAE (Pharmacia) anion chromatography and affinity chromatography using Affi-Gel Blue (BioRad). Protein concentrations were determined by the method of Bradford[37] using BSA as a standard. All preparations were 98% free of contaminating enzymes as judged by Coomassie Blue staining following SDS−PAGE.

Crystallization of *wt*IDH and IDH (K100M). Concentrated protein solutions of *wt*IDH (35 mg/mL) and IDH (K100M) (45 mg/mL) were diluted to 20 mg/mL in a storage buffer solution containing 0.9 mM citric acid, 3.5 mM Na_2HPO_4 pH 6.0, 100 mM NaCl, 0.02% NaN_3 and 2 mM DTT. Crystal growth optimization was carried out using the hanging drop vapor diffusion method by screening 24 different crystallization solutions with varying pH and $(NH_4)_2SO_4$ concentrations close to the conditions established by Hurley and co-workers.[38] The best crystallizations were obtained in a solution of 1.85M $(NH_4)_2SO_4$, 50 mM citric acid/Na_2HPO_4, 0.1 M NaCl and 0.2 M DTT at pH 5.8 for *wt*IDH and at pH 5.2 for IDH (K100M). Protein crystals for ligand soaking and diffraction data collection were also obtained by the hanging drop vapor diffusion method. Two μL drops were set up at 293 K in a XRL 24-well crystallization plate (Molecular Dimensions), by mixing native and mutant protein solutions with their respective crystallization solutions in a 1:1 ratio of protein to reservoir solution, and equilibrated against 500 μL of crystallization solution in the reservoir. Single crystals with tetragonal bipyramidal shape developed within 5 days, reaching dimensions of 500 μm × 200 μm × 100 μm for *wt*IDH and of 300 μm × 150 μm × 75 μm for IDH (K100M).

Crystal Soaking Procedure. Crystals of *wt*IDH and IDH (K100M) were transferred from their mother liquor to the final soaking solution in either one or two steps. In the two-step procedure the crystals were first soaked in Solution 1 (1.58 M $(NH_4)_2SO_4$, 156 mM NaHEPES pH 6.0, 52 mM Ca^{2+} or Mg^{2+}, 300 mM ICT) and then transferred to Solution 2 (1.58 M $(NH_4)_2SO_4$, 156 mM NaHEPES/MES pH 7.5−8.0, 52 mM Ca^{2+} or Mg^{2+}, 300 mM ICT or α-KG, 400−500 mM $NADP^+$ or NADPH or thio-$NADP^+$), whereas the one-step procedure involved only Solution 2. All the soaks were done at 293 K. Crystals were then cryo-protected by transferring them directly into an artificial mother liquor with the same composition as that of soaking solution 2 supplemented with 25% glycerol, and flash-cooled in liquid nitrogen prior to data collection. For each data set, the composition of the soaking solutions and the final ligand concentrations, as well as the duration of each soak, are described in Table S1.

The following stock solutions were used to prepare the soaking solutions: 1 M NaHEPES pH 7.5 (Sigma-Aldrich), 1 M MES-NaOH (Sigma-Aldrich) pH 6.3, 2 M $MgCl_2$ (Sigma-Aldrich); 2 M $CaCl_2$ (Sigma-Aldrich); 2 M ICT (Fluka) in 11% NH_4OH (Merck) pH 6.0; 0.5 M α-KG (Sigma-Aldrich) in 0.1 M MES-NaOH (Sigma-Aldrich) pH 6.3; and 0.24 M β-NADPH (Sigma-Aldrich) in 166 mM α-KG (Sigma-Aldrich), 166 mM MES-NaOH (Sigma-Aldrich) pH 6.3 and 1.54 M

Table 1. Data Collection and Processing Statistics[a]

data sets	wt [Ca²⁺:ICT:NADP⁺]	K100M [Mg²⁺:ICT:NADP⁺] x1	K100M [Mg²⁺:ICT:NADP⁺] x2	K100M [Ca²⁺:α-KG:NADPH]	K100M [Mg²⁺:ICT:thio-NADP⁺]	wt [Ca²⁺:ICT:thio-NADP⁺]
beamline	in house	ESRF ID23-1	ESRF ID14-4	in house	SLS PXIII	SLS PXIII
detector	Proteum Pt135	ADSC Q315r	ADSC Q315r	Proteum Pt135	Mar225	Mar225
processing packages	ProteumSuite, XPREP, CCP4	XDS, CCP4	XDS, CCP4	Proteum Suite, XPREP, CCP4	XDS, CCP4	XDS, CCP4
wavelength (Å)	1.5418	0.9795	0.9535	1.5418	0.9792	0.9792
space group			$P4_32_12$			
cell parameters (Å)	a = b = 105.30, c = 145.72	a = b = 103.58, c = 149.68	a = b = 105.79, c = 145.49	a = b = 103.68, c = 149.58	a = b = 103.05, c = 150.34	a = b = 104.01, c = 149.56
resolution (Å)	47.10–1.90 (2.00–1.90)	50.00–1.80 (1.91–1.80)	60.00–2.69 (2.85–2.69)	46.37–2.30 (2.40–2.30)	48.74–1.90 (2.01–1.90)	50.0–1.80 (1.91–1.80)
no. observations	370445 (30740)	851107 (128548)	203269 (30161)	557631 (40200)	468880 (71214)	552349 (85244)
no. unique reflections	65181 (9149)	75372 (11833)	23556 (3636)	36981 (4332)	64372 (9910)	76263 (11806)
completeness (%)	99.9 (100.0)	99.7 (98.5)	99.5 (97.5)	100.0 (100.0)	99.4 (96.1)	99.4 (96.7)
multiplicity	5.7 (3.4)	11.3 (10.8)	8.6 (8.3)	15.1 (9.3)	7.3 (7.2)	7.2 (7.2)
$<I/\sigma(I)>$	11.2 (1.7)	12.3 (2.6)	15.2 (2.8)	24.8 (6.1)	18.2 (3.2)	17.7 (2.7)
R-merge (%)[b]	11.0 (54.0)	12.6 (70.8)	12.5 (83.5)	8.3 (31.4)	7.6 (54.5)	6.7 (62.6)
R-meas (%)[b]		13.1 (74.2)	13.3 (89.0)		8.2 (58.7)	7.2 (67.4)
R-pim (%)[b]	4.9 (34.8)			2.1 (10.8)		
Wilson B (Å²)	18.7	30.6	51.6	32.7	31.2	31.8

[a]Values in parentheses refer to the highest resolution shell. [b]R-merge = merging R-factor, $(\Sigma_{hkl} \Sigma_i |I_i(hkl) - <I(hkl)>|)/(\Sigma_{hkl} \Sigma_i I(hkl)) \times 100\%$; R-meas = multiplicity independent R-factor, $\Sigma_{hkl} [N_{hkl}/(N_{hkl}-1)]^{1/2} \Sigma_i |I_i(hkl) - <I(hkl)>|/\Sigma_{hkl} \Sigma_i I_i(hkl) \times 100\%$; R-pim = precision independent R-factor, $\Sigma_{hkl} [1/(N_{hkl}-1)]^{1/2} \Sigma_i |I_i(hkl) - <I(hkl)>|/\Sigma_{hkl} \Sigma_i I_i(hkl) \times 100\%$,[65] where $I_i(hkl)$ is the observed intensity, $<I(hkl)>$ is the average intensity of multiple observations from symmetry-related reflections, and N_{hkl} is their multiplicity.

Table 2. Refinement Statistics

	wt [Ca²⁺:ICT:NADP⁺]	K100M [Mg²⁺:ICT:NADP⁺] x1	K100M [Mg²⁺:ICT:NADP⁺] x2	K100M [Ca²⁺:α-KG:NADPH]	K100M [Mg²⁺:ICT:thio-NADP⁺]	wt [Ca²⁺:ICT:thio-NADP⁺]
resolution limits (Å)	44.81–1.90 (1.97–1.90)	46.34–1.80 (1.86–1.80)	52.90–2.70 (2.80–2.70)	44.30–2.30 (2.38–2.30)	48.90–1.90 (1.97–1.90)	46.5–1.80 (1.86–1.80)
R-factor[a]	0.190 (0.351)	0.170 (0.253)	0.160 (0.230)	0.175 (0.233)	0.165 (0.242)	0.183 (0.270)
no. reflections[b]	61806 (6069)	71597 (6867)	22359 (2362)	34197 (3324)	61051 (5951)	72371 (6824)
free R-factor[c]	0.224 (0.347)	0.19 (0.284)	0.210 (0.292)	0.210 (0.278)	0.181 (0.263)	0.204 (0.286)
no. reflections[b]	3272 (324)	3768 (358)	1195 (119)	1822 (203)	3235 (308)	3802 (331)
overall coordinate error estimate (Å)[d]	0.58	0.38	0.66	0.64	0.42	0.37
Model Completeness and Composition (%)						
regions omitted		Met 1	Met 1	Met 1	Met 1	Met 1
Mg²⁺/Ca²⁺	Ca²⁺	Mg²⁺	Mg²⁺	Ca²⁺	Mg²⁺	Ca²⁺
NADP⁺/NADPH/thio-NADP⁺	NADP⁺	NADP⁺	NADPH	NADPH	thio-NADP	thio-NADP
NMN moiety	1	1				
A2P moiety	1	1	1	1		
ICT/α-KG	ICT	ICT	α-KG	α-KG	ICT	ICT
SO₄³⁻	1	1		1		1
loop conformation	"fully closed"	"quasi-closed"	"fully closed"	"quasi-closed"	"quasi-closed"	"quasi-closed"
non-hydrogen protein atoms	3674	3814	3412	3716	3809	3818
disordered residues	5	6		7	9	7
solvent molecules	374	504	127	429	490	507
Mean B Values (Å²)[e]						
protein main-chain	27.2	29.5	25.3	27.08	27.8	29.07
protein side-chain	30.0	33.4	29.5	30.40	31.7	32.57
ions and ligands	27.7	40.7	40.2	47.8	38.3	33.0
solvent	38.7	40.1	27.4	42.4	42.4	42.7
Model rms Deviations from Ideality						
bond lengths (Å)	0.007	0.007	0.008	0.008	0.007	0.007
bond angles (°)	1.088	1.041	1.139	1.101	1.079	1.086
chiral centers (Å³)	0.070	0.072	0.069	0.073	0.073	0.075
planar groups (Å)	0.004	0.004	0.004	0.005	0.005	0.004
Model Validation[f]						
% Ramachandran outliers	0.0	0.0	0.5	0.0	0.0	0.0
% Ramachandran favored	96.9	97.6	96.1	96.9	96.9	97.1
% rotamer outliers	0.0	0.9	2.4	0.9	0.3	0.3
C[β] outliers	0	0	0	0	0	0
clash score	6.00	7.01	9.37	8.81	5.55	6.30
PDB accession ID	4aj3	4ajs	4ajr	4ajc	4ajb	4aja

[a]R-factor $= \Sigma_{hkl}||F_o| - |F_c||/\Sigma_{hkl}|F_o|$, where $|F_o|$ and $|F_c|$ are the observed and calculated structure factor amplitudes, respectively. [b]No $\sigma(F_o)$ cutoff. [c]Cross-validation R-factor computed from a randomly chosen subset of 5% of the total number of reflections were not used during the refinement. [d]Maximum-likelihood estimate. [e]Calculated from isotropic or equivalent isotropic B-values. [f]Calculated with MolProbity.[48]
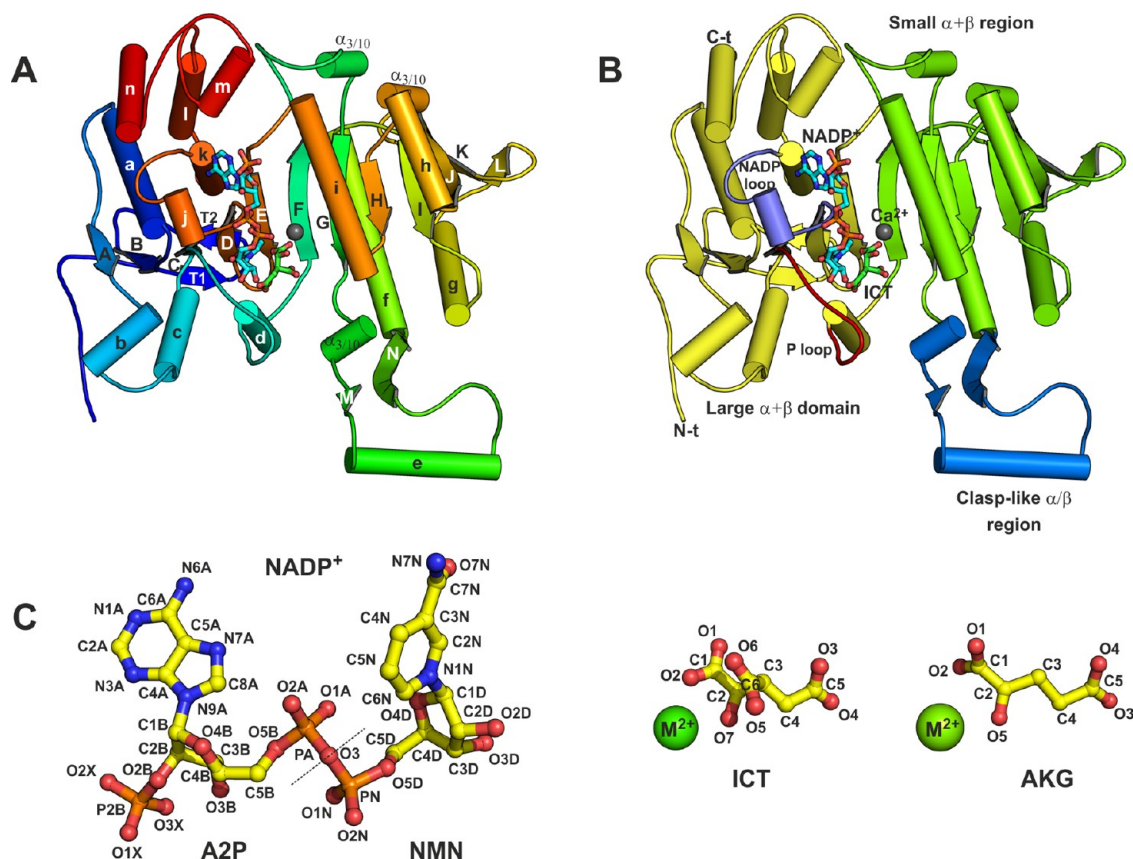
Figure 1. The *E. coli* IDH monomer and its ligands. (A) Secondary structure: ribbon representation of the IDH monomer in the *wt* [Ca^{2+}:ICT:NADP$^+$] crystal structure, rainbow-color coded from N-terminal (blue) to C-terminal (red). The secondary structure elements are labeled according to Hurley's scheme: β-strands are denoted by capital letters and α-helices are labeled in lowercase letters.[38] The T1 and T2 elements indicate the N-terminal β-hairpin. (B) Domain structure: ribbon representation of the IDH monomer in the *wt* [Ca^{2+}:ICT:NADP$^+$] crystal structure, color coded according to the domain structure. Domain I (large α + β domain, residues 1−124 and 318−416) is colored light yellow. Domain II comprises the small α/β region (residues 125−157 and 203−317) represented in light green and a α/β clasp-like region (residues 158−202) displayed in marine blue. The phosphorylation and NADP-binding loops are highlighted in red and slate blue, respectively. The NADP$^+$ and ICT ligands are drawn in ball-and-stick and Ca^{2+} is depicted as a sphere. Atom colors are: gray for calcium, orange for phosphorus, blue for nitrogen and red for oxygen; carbon atoms from NADP$^+$ and ICT are colored cyan and green, respectively. (C) Ball-and-stick diagrams of the NADP$^+$, ICT:M^{2+}, and AKG:M^{2+} ligands in the IDH crystal structures showing the atom labeling scheme used in the text. M^{2+} represents either one of the Mg^{2+} or Ca^{2+} metal ions. In thio-NADP$^+$ the sulfur atom S1 replaces O17. The dashed line at atom O3 in NADP$^+$ marks the division between the A2P and the NMN moieties.

(NH$_4$)$_2$SO$_4$ (Merck). Na$_2$β-NADP$^+$ (Fluka) and Naβ-thio-NADP$^+$ (Sigma-Aldrich) were added directly to soaking solution 1 (see Table S1).

Data Collection and Processing. Data sets of the different IDH crystal soaks were collected at 100 K using different X-ray sources and detector systems. The *wt* [Ca^{2+}:ICT:NADP$^+$] and K100M [Ca^{2+}:α-KG:NADPH] data sets were measured *in-house*, using a Bruker-AXS Proteum Pt135 CCD detector system coupled to a Bruker-AXS Microstar-I rotating anode X-ray generator with Montel mirrors. The data were integrated with SAINT and scaled with SADABS as part of the Bruker-AXS Proteum Software Suite. Diffraction data statistics were obtained with XPREP (Bruker-AXS) and are listed in Table 1. The K100M [Mg^{2+}:ICT:NADP$^+$] x1 and K100M [Mg^{2+}:ICT:NADP$^+$] x2 data sets were collected at the ESRF (Grenoble, France) ID14−4 and ID23−1 beamlines respectively, using an ADSC Quantum Q315r detector. The K100M [Mg^{2+}:ICT:thio-NADP$^+$] and the *wt* [Ca^{2+}:ICT:thio-NADP$^+$] data sets were recorded at the SLS (Villigen, Switzerland) PXIII beamline, using a MAR225 detector. For the data sets collected at

synchrotron X-ray sources, the diffraction images were processed with XDS,[39] and the data collection statistics are included in Table 1. All diffraction data were further processed with the CCP4 Program Suite.[40] Two preliminary data sets, replicates of *wt* [Ca^{2+}:ICT:NADP$^+$] and K100M [Mg^{2+}:ICT:NADP$^+$] x1 data sets, were initially collected *in-house* at 293 K and the respective crystal structures were solved by Molecular Replacement with PHASER,[41] using the coordinates of the PDB entry 1ai2[27] as the search model. The solutions were partially refined (our unpublished results) and subsequently used as search models to solve the crystal structures herein described by the Molecular Replacement with PHASER. Although Matthews coefficient calculations[42] suggested the presence of two molecules in the asymmetric unit of all crystal structures, with V_m values of about 2.2 Å^3 Da^{-1} and a predicted solvent content of about 45%, the results of the Molecular Replacement calculations showed that, as in all *Eco*IDH crystal structures reported to date (see Results), only one *wt*IDH or IDH (K100M) monomer was present in the asymmetric unit of each crystal structure, corresponding to V_m

Table 3. Secondary Structure Matching Comparisons for *E. coli* IDH[a]

PDB id	ref	resolution (Å)	year	Rmsd-1 (Å)	Rmsd-2 (Å)	ligands	
				Escherichia coli K12			
4aj3	this work	1.90	2012	0.00	1.01	Ca^{2+}, ICT, $NADP^+$	
4ajr	this work	2.70	2012	0.26	1.03	Mg^{2+}, ICT, $NADP^+$	
4ajs	this work	1.80	2012	1.01	0.00	Mg^{2+}, ICT, $NADP^+$	SO_4^{2-}
4aja	this work	1.80	2012	0.94	0.19	Ca^{2+}, ICT, thio-$NADP^+$	SO_4^{2-}
4ajb	this work	1.90	2012	1.12	0.18	Mg^{2+}, ICT, thio-$NADP^+$	SO_4^{2-}
4ajc	this work	2.30	2012	0.95	0.21	Ca^{2+}, α-KG, NADPH	SO_4^{2-}
1sjs	53	2.42	1997	2.36	2.08		
3icd	38	2.50	1989	0.98	0.33		
4icd	66	2.50	1990	0.97	0.34		
5icd	22	2.50	1990	1.04	0.32	Mg^{2+}, ICT	
6icd	22	2.80	1990	0.96	0.36		
7icd	22	2.40	1990	0.95	0.36		
8icd	22	2.50	1990	1.00	0.32	Mg^{2+}, ICT	
9icd	13	2.50	1991	0.90	0.35	$NADP^+$	
1ika	67	2.70	1993	1.16	0.85	Ca^{2+}, α-KG	
1idc	23	2.50	1995	0.95	0.45	Mg^{2+}, OXS	
1idd	23	2.50	1995	1.04	0.46		
1ide	23	2.50	1995	0.99	0.48	Mg^{2+}, ICT, $NADP^+$	
1idf	23	2.50	1995	0.99	0.51		
1gro	24	2.50	1995	1.01	0.33	Mg^{2+}, ICT	
1grp	24	2.50	1996	1.01	0.31	Mg^{2+}, ICT	
1iso	68	1.90	1996	1.05	0.37	NAD^+	SO_4^{2-}
1ai2	27	1.90	1997	1.05	0.38	Ca^{2+}, ICT, $NADP^+$	
1ai3	27	1.90	1997	1.03	0.37	Mg^{2+}, ICT, $NHDP^+$	
1bl5	28	2.50	1998	1.04	0.39	Mg^{2+}, α-KG, NADPH	
1p8f	69	1.85	2000	1.03	0.16	Mg^{2+}, ICT	SO_4^{2-}
1pb1	69	1.70	2000	0.97	0.21	ICT	SO_4^{2-}
1pb3	70	1.70	2000	0.98	0.19		SO_4^{2-}
1cw1	25	2.10	2000	1.01	0.24	Mn^{2+}, ICT	SO_4^{2-}
1cw4	25	2.10	2000	1.03	0.24	Mn^{2+}, α-KG	SO_4^{2-}
1cw7	25	2.60	2000	1.01	0.27	Mg^{2+}, ICT	SO_4^{2-}
1hj6	29	2.00	2001	0.47	0.82	Mg^{2+}, IPM, $NADP^+$	
3lcb:C	55	2.90	2010	2.24	2.21		
3lcb:D	55	2.90	2010	2.44	2.08		
				Acidithiophilus thiooxidans (UNIPROT Q8GAX0), 60.1% Identity			
2d4v:A	56	1.90	2008	0.81	1.36	citrate, NAD^+	
2d4v:B				0.87	1.37	citrate, NAD^+	
2d4v:C				0.77	1.30	citrate, NAD^+	
2d4v:D				0.76	1.38	citrate, NAD^+	
				Burkholderia pseudomallei Strain 1710b (UNIPROT Q3JV82), 74.2% identity			
3dms	71	1.65	2011	0.92	0.62		
				Aeropyrum pernix ATCC 700893 (UNIPROT Q9YE81), 45.2% identity			
1xkd:A	20	2.3	2005	2.24	1.94	Ca^{2+}, ICT, $NADP^+$	
1xkd:B				0.99	1.33	ICT, $NADP^+$	
				Bacillus subtilis Strain 168 (UNIPROT P39126), 65.0% identity			
1hqs:A	72	1.55	2001	1.08	0.95	ICT	
1hqs:B				1.22	0.70	ICT	

[a]Rmsd-1 is calculated between $C^α$-atoms of matched residues at best 3D superposition of the query 4aj3 and target structures; Rmsd-2 is calculated between $C^α$-atoms of matched residues at best 3D superposition of the query 4ajs and target structures; ligand abbreviations: ICT, 2R,3S-isocitric acid/isocitrate; $NADP^+$, β-nicotinamide adenine dinucleotide phosphate; NADPH, β-nicotinamide adenine dinucleotide phosphate (reduced); thio-$NADP^+$, β-thio-nicotinamide adenine dinucleotide phosphate; NHDP, β-nicotinamide-(6-deamini-6-hydroxy-adenine)-dinucleotide phosphate; α-KG, α-ketoglutarate or 2-oxoglutarate; OXS, 2-oxosuccinate; IPM, isopropylmalate; NAD^+, β-nicotinamide adenine dinucleotide.

values and estimated solvent contents of ca. 4.5 $Å^3$ Da^{-1} and 72.4%, respectively.

Crystallographic Refinement. The structures were refined using the amplitude-based Maximum-Likelihood target function with automatic weight optimization procedure as implemented through the graphics user interface of the PHENIX v.1.6.4 software package.[43] The initial refinement step consisted of five macrocycles, the first of which comprised a rigid body refinement followed by individual coordinate and isotropic atomic displacement parameter (ADP) refinement. In the second and fourth macrocycles, a simulated annealing refinement (Cartesian and torsion angles) was carried out using

Table 4. Summary of DynDom calculations for *E. coli* IDH Crystal Structures

PDB id	ref	Domain I rmsd (Å)	Domain II rmsd (Å)	rotation (deg)	hinge residues	conformation	NADP loop	P-loop
1sjs	53			0		open	out	out
4aj3	this work	1.01	0.59	24.4	125−126, 323−329	fully closed	in	in
4ajr	this work	0.99	0.56	24.5	125−127, 323−329	fully closed	in	in
4ajs	this work	0.54	0.41	18.6	126−127, 322−327	quasi-closed	out	out
4aja	this work	0.53	0.40	18.7	126−127, 324−328	quasi-closed	out	out
4ajb	this work	0.57	0.42	18.3	126−127, 323−327	quasi-closed	out	out
4ajc	this work	0.53	0.41	18.8	126−127, 323−325	quasi-closed	out	out
3icd	38	0.56	0.36	19.7	126−128, 323−324	quasi-closed	out	out
4icd	66	0.56	0.36	19.8	126−128, 323−324	quasi-closed	out	out
5icd	22	0.56	0.43	19.4	125−127, 323−324	quasi-closed	out	out
6icd	22	0.58	0.38	19.7	125−128, 323−324	quasi-closed	out	out
7icd	22	0.56	0.38	19.8	126−128, 323−324	quasi-closed	out	out
8icd	22	0.56	0.41	19.5	126−128, 324−327	quasi-closed	out	out
9icd	13	0.55	0.36	19.8	126−127, 323−324	quasi-closed	out	out
1ika	67	0.97	0.84	20.0	126−127, 136, 323−328	quasi-closed	out	out
1idc	23	0.59	0.44	20.0	126−128, 134, 323−324	quasi-closed	out	out
1idd	23	0.67	0.45	19.7	126−127, 323−324	quasi-closed	out	out
1ide	23	0.66	0.45	19.7	126−127, 323−328	quasi-closed	out[a]	out
1idf	23	0.60	0.48	20.0	126−127, 323−328	quasi-closed	out	out
1gro	24	0.56	0.38	19.5	126−128, 323−328	quasi-closed	out	out
1grp	24	0.55	0.39	19.5	126−128, 323−328	quasi-closed	out	out
1iso	68	0.65	0.40	19.2	126−128, 323−324	quasi-closed	iso	out
1ai2	27	0.65	0.42	19.2	126−128, 323−329	quasi-closed	out	out
1ai3	27	0.65	0.41	19.2	126−129, 321−328	quasi-closed	out	out
1bl5	28	0.60	0.47	19.2	126−127, 324−328	quasi-closed	out	out
1p8f	69	0.57	0.43	18.6	126−127, 322−324	quasi-closed	out	out
1pb1	69	0.57	0.41	18.8	126−128, 322−324	quasi-closed	out	out
1pb3	70	0.54	0.38	18.8	126−128, 319, 322−324	quasi-closed	out	out
1cw1	25	0.57	0.38	18.6	126−128, 319, 322−324	quasi-closed	out	out
1cw4	25	0.57	0.38	18.6	126−128, 319, 322−324	quasi-closed	out	out
1cw7	25	0.59	0.41	18.6	126−128, 319, 322−328	quasi-closed	out	out
1hj6	29	0.78	0.57	19.7	126−128, 323−324	quasi-closed	out	out
3lcb:C	55	1.29	0.38	2.4	b	open	out	in
3lcb:D	55	1.28	0.38	1.4	b	open	out	in

[a]But with a different conformation. [b]DynDom failed due to very similar domain orientations. These values were obtained with LSQKAB.

the default parameters, followed by individual coordinate and ADP refinement of individual isotropic B-factors. Monomer library descriptions for new ligands were created with LIBCHECK[44] through the smiles translator interface in Coot.[45] Ligand restraints were further reviewed using JLigand.[46] During refinement, the models were periodically inspected and corrected with Coot against σ_A-weighted $2|F_o| − |F_c|$ and $|F_o| − |F_c|$ electron density maps. Inclusion of ordered solvent molecules was done with ARP/wARP,[47] followed by inspection in Coot. In the final refinement, automatic atom occupancy refinement was included in the protocol. The stereochemical quality of each model was assessed with MolProbity.[48] A summary of the refinement statistics, model composition and stereochemical quality is presented in Table 2. Coordinates and structure factors were deposited in the Protein Data Bank in Europe.[49] The coordinate accession codes are also included in Table 2.

Structure Analysis. Structures were superimposed at their corresponding domains I and II (see Structural Overview in the Results for definitions of domains I and II), and rms deviations between superimposed atoms were calculated using the CCP4 suite program LSQKAB.[50] Domain rotations and hinge points for *Eco*IDH crystal structures were determined using the program DynDom[51] as implemented through the CCP4i

graphics user interface[52] with default parameters. Using the "open" apo-form of *Eco*IDH (PDB 1sjs)[53] as a reference, the small domains were first aligned and then the positions of the large domains were compared. DynDom calculations failed for small rigid body rotations and so LSQKAB calculations[50] in CCP4i were used to first superimpose the small domains and then use the resulting transformed coordinate file to superimpose the large domains. LSQKAB calculations were also used to compare crystal structures from different organisms. The analysis of the residues involved in the binding of NADP$^+$/ NADPH and ICT/α-KG (as a metal-bound ligand complex), was done by least-squares superposition of domains I and II respectively, using the CCP4 suite program LSQKAB. The calculation of the rms deviations between the superimposed ligands was done by matching them using the least-squares superposition function implemented in Coot.[45] Comparison of the IDH structures reported herein with their closest homologues was carried out using the Secondary Structure Matching (SSM) method[54] as implemented in the CCP4 suite. Distances and angles were calculated using Coot. Crystal-packing contacts were determined with the CCP4 suite program NCONT. Most of the CCP4 suite programs were used through the CCP4 graphical user interface.[52]
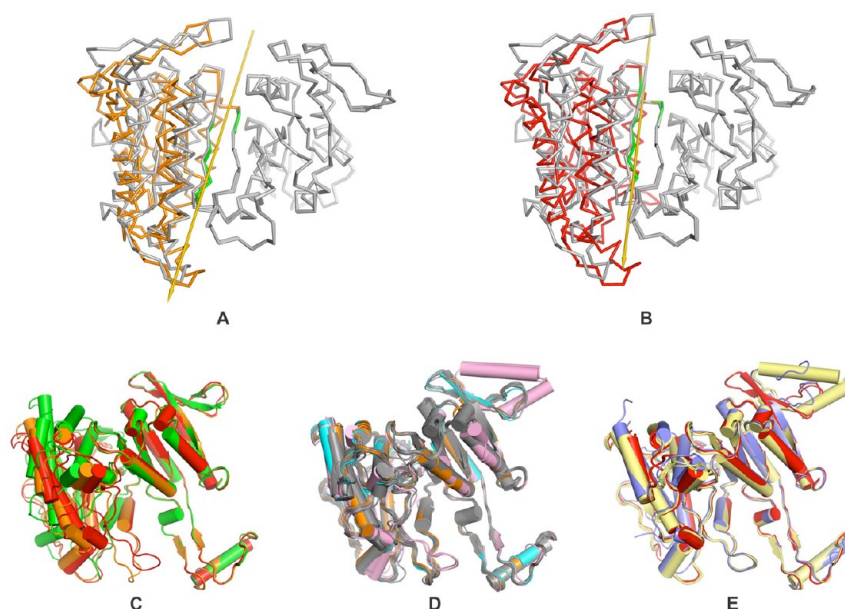
Figure 2. Interdomain hinge dynamics in *Eco*IDH. (A) Ribbon diagram showing the large domain rotation between the open (PDB 1sjs, light gray) and quasi-closed (K100M [Mg^{2+}:ICT:NADP$^+$] x1 complex, orange) conformations of *Eco*IDH. The rotation axis determined with DynDom is drawn in gold and the corresponding hinge residues are colored green. For clarity, the small domain is shown in light gray. (B) Ribbon diagram showing the large domain rotation between the open (PDB 1sjs, light gray) and fully closed (*wt* [Ca^{2+}:ICT:NADP] *pseudo*-Michaelis complex, red) conformations of *Eco*IDH. The rotation axis determined with DynDom is drawn in gold and the corresponding hinge residues are colored green. For clarity, the small domain is shown in light gray. (C) Cartoon diagram of selected *Eco*IDH monomers from this work, illustrating the rigid-body hinge motion of the large domains after superposition of the small domains. The open conformation (PDB 1sjs) is represented in green, the quasi-closed conformation of the K100M [Mg^{2+}:ICT:NADP$^+$] x1 complex is colored orange, and the fully closed conformation of the *wt* [Ca^{2+}:ICT:NADP] *pseudo*-Michaelis complex is displayed in red. (D) Cartoon diagram of IDH monomers in the quasi-closed conformation, after superposition of the small domains. The four complexes from this work are colored orange, the other *Eco*IDH monomers are shown in gray, *B. pseudomallei* IDH is displayed in cyan and *B. subtilis* IDH chains A and B are represented in pink. (E) Cartoon diagram of IDH monomers in the fully closed conformation, after superposition of the small domains. The two complexes from this work are colored red, *A. pernix* IDH chain B is shown in slate blue and the 4 chains of *A. thiooxidans* IDH are represented in pale yellow. Panels A and B are drawn in the same orientation, different from that of panels C–E, to better show the location of the hinge residues and the orientation of the rotation axes.

Figures were generated using the PyMOL Molecular Graphics System, Version 1.4.1 (Schrödinger, LLC).

■ RESULTS

Structural Overview. Both *wt*IDH and IDH (K100M) crystallized in the tetragonal space group $P4_32_12$ with one monomer in the asymmetric unit (Figure 1A). The biological unit is a homodimer with subunits related by a binary crystallographic axis (Figure S1). The monomers fold as previously described[38] with a large $\alpha + \beta$ domain (residues 1–124 and 318–416) and a small α/β domain (residues 125–317) that includes a distinctive clasp-like α/β subdomain (residues 158–202) (Figure 1B). Secondary structure elements are referenced using Hurley's nomenclature[38] with residues in the second subunit denoted by an asterisk (*).

We designate different data sets, and the corresponding crystal structures, based on the different protein crystals and ligands in which they were soaked: A [B:C:D], with A either *wt* for *wt*IDH or K100M for IDH (K100M); B either Mg^{2+} or Ca^{2+}; C either isocitrate (ICT) or α-ketoglutarate (α-KG); and D either NADP$^+$, thio-NADP$^+$ or NADPH. The suffixes x1 and x2 distinguish data sets collected from different crystals of a given soak. Note that α-ketoglutarate is bound in the K100M [Mg^{2+}:ICT:NADP$^+$] x2 ternary product complex, the enzyme having turned over the substrate *in crystallum*.

To date, there are 27 crystal structures of *E. coli* isocitrate dehydrogenase in the Protein Data Bank (Table 3). Secondary structure matching against the entire PDB, carried out with SSM[54] as implemented at the European Bioinformatics Institute (http://www.ebi.ac.uk/PDBeFold) and using coordinates from the *wt* [Ca^{2+}:ICT:NADP] and K100M [Mg^{2+}:ICT:NADP$^+$] x1 crystal structures, also recovered several IDHs from other organisms with high structural similarity to *Eco*IDH. The four crystal structures displaying the lowest rms deviations were selected for further analysis and comparison with our *Eco*IDH crystal structures (Table 3).

We first describe the large intra- and interdomain conformational changes upon ligand binding and then describe the details of the active site in the catalytically productive "fully closed" conformations of *Eco*IDH.

Intradomain Dynamics. Least-squares superpositions of the large domain in all published crystal structures of *Eco*IDH against that of the apo-isoform (PDB 1sjs)[53] (Table 4) show larger variations (0.5–1.3 Å C$^\alpha$ rms deviations) than similar calculations for the small domain (0.3–0.4 Å C$^\alpha$ rms deviations, with the notable exception of 0.8 Å for 1ika). In the large domain, the main structural differences are located in those residues that define the adenosine 2′,5′-diphosphate binding pocket (residues 336–352 of the NADP-binding loop, residues 100–113 of the phosphorylation loop, residues 114–122 at the N-terminus of helix "d" and residues 71–79 that comprise helix "l"). In the small domain, deviations are confined to the loop linking β-strand "K" to the disordered β-strand "L" (residues 259–261) at the end of the sheet. Local structural differences attributable to crystal packing are present only at the interface

Table 5. Summary of Domain Motion Calculations for Selected IDHs

PDB id	ref	Domain II rmsd (Å)	Domain I rmsd (Å)	rotation (deg)	conformation	NADP loop	P-loop
			Escherichia coli				
1sjs	53			0°	open		
4aj3	this work	0.41	1.06	24.3	fully closed	in	in
4ajr	this work	0.37	1.05	24.5	fully closed	in	in
4ajs	this work	0.36	0.56	18.6	quasi-closed	out	out
4aja	this work	0.33	0.56	18.7	quasi-closed	out	out
4ajb	this work	0.37	0.60	18.3	quasi-closed	out	out
4ajc	this work	0.35	0.54	18.9	quasi-closed	out	out
1hj6	29	0.41	0.85	21.5	quasi-closed	out	in
9icd	13	0.29	0.57	19.7	quasi-closed	out	out
			Acidithiophilus thiooxidans				
2d4v:A	56	0.50	1.38	26.0	fully closed	in	in
2d4v:B		0.48	1.37	26.1	fully closed	in	in
2d4v:C		0.51	1.36	25.0	fully closed	in	in
2d4v:D		0.50	1.36	25.7	fully closed	in	in
			Burkholderia pseudomallei				
3dms	71	0.47	0.57	19.5	quasi-closed	out	out[a]
			Aeropyrum pernix				
1xkd:A	20	0.63	1.01	2.2	open	in	out[a]
1xkd:B		0.63	1.34	23.1	fully closed	in	in
			Bacillus subtilis				
1hqs:A	72	0.44	0.74	22.1	quasi-closed	out	in
1hqs:B		0.43	0.62	19.0	quasi-closed	out	in

[a]Incomplete loop in coordinate file.
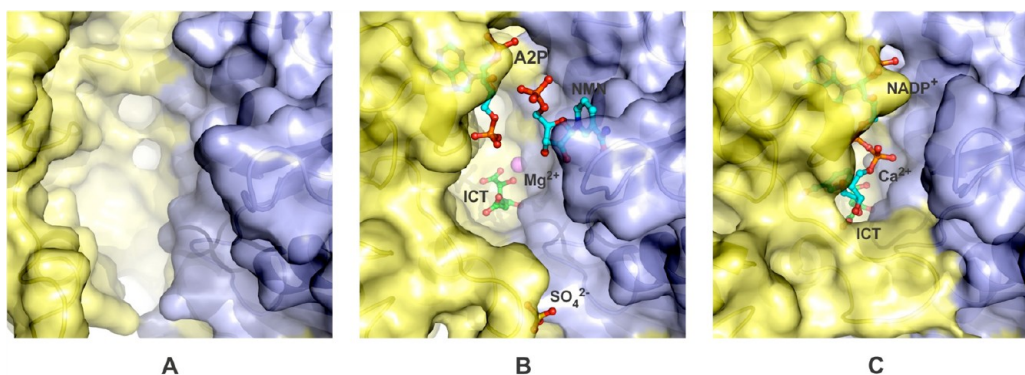
Figure 3. Closure of the active site as the large domain rotates from the "open" to the "quasi-closed" and "fully closed" positions. (A) The "open" form (PDB 1sjs).[53] (B) The "quasi-closed" form, represented by the K100M [Mg²⁺:ICT:NADP⁺] x1 crystallographic dimer. (C) The catalytically competent "fully closed" conformation, represented by the *wt* [Ca²⁺:ICT:NADP⁺] crystallographic dimer. The protein chains are shown as cartoons. The respective molecular surfaces are represented as semitransparent and were calculated using a solvent probe radius of 1.4 Å. The surface of monomer A is colored light yellow and that of symmetry-related monomer B is displayed in light blue. Ligands are shown as ball-and-stick and Mg²⁺ and Ca²⁺ ions drawn as spheres. Atom colors are violet for magnesium, gray for calcium, yellow for sulfur, orange for phosphorus, blue for nitrogen, red for oxygen, green for carbon atoms in ICT and cyan for carbon atoms in NADP⁺, A2P, and NMN.

defined by helix "h" and the phosphorylation loop of a second homodimer related by crystallographic symmetry. We thus attribute intramolecular structural rearrangements to substrate binding during the soaking assays.

Interdomain Hinge Dynamics. Changes between the conformational states of *Eco*IDH (classified as "open", "quasi-closed", and "fully closed") are attributable to rigid body rotations about an axis that lies approximately parallel to, and between, β-strands "E" and "F" located between the large and small domains (Figure 2A,B). *Eco*IDH apo-isoform (PDB 1sjs),[53] *Eco*IDH bound to *E. coli* isocitrate dehydrogenase kinase/phosphatase (PDB 3lcb)[55] and *Aeropyrum pernix* IDH (PDB 1xkd, chain A)[20] adopt the "open" conformation. The vast majority of IDH structures listed in Tables 4 and 5,

including those purporting to represent or mimic *pseudo*-Michaelis complexes of *Eco*IDH (PDB 1ide,[23] 1ai2 and 1ai3,[27] and 1hj6[29]), exhibit a nonproductive "quasi-closed" conformation, intermediate between the "open" and "fully closed" forms, with the large domain rotated by ca. 20° relative to the "open" apo-*Eco*IDH structure. In our "quasi-closed" structures and several others (Table 3) a sulfate ion from the crystallization solution interacts with the phosphorylation loop, possibly contributing to the incomplete closure of the large domain. Our "fully closed" *wt* [Ca²⁺:ICT:NADP⁺] *pseudo*-Michaelis and K100M [Mg²⁺:ICT:NADP⁺] x2 ternary product complexes show ca. 24.5° large domain rotations relative to the "open" conformation (Figure 2E). Though they differ in detail, both are similar to the nonproductive ternary complexes of
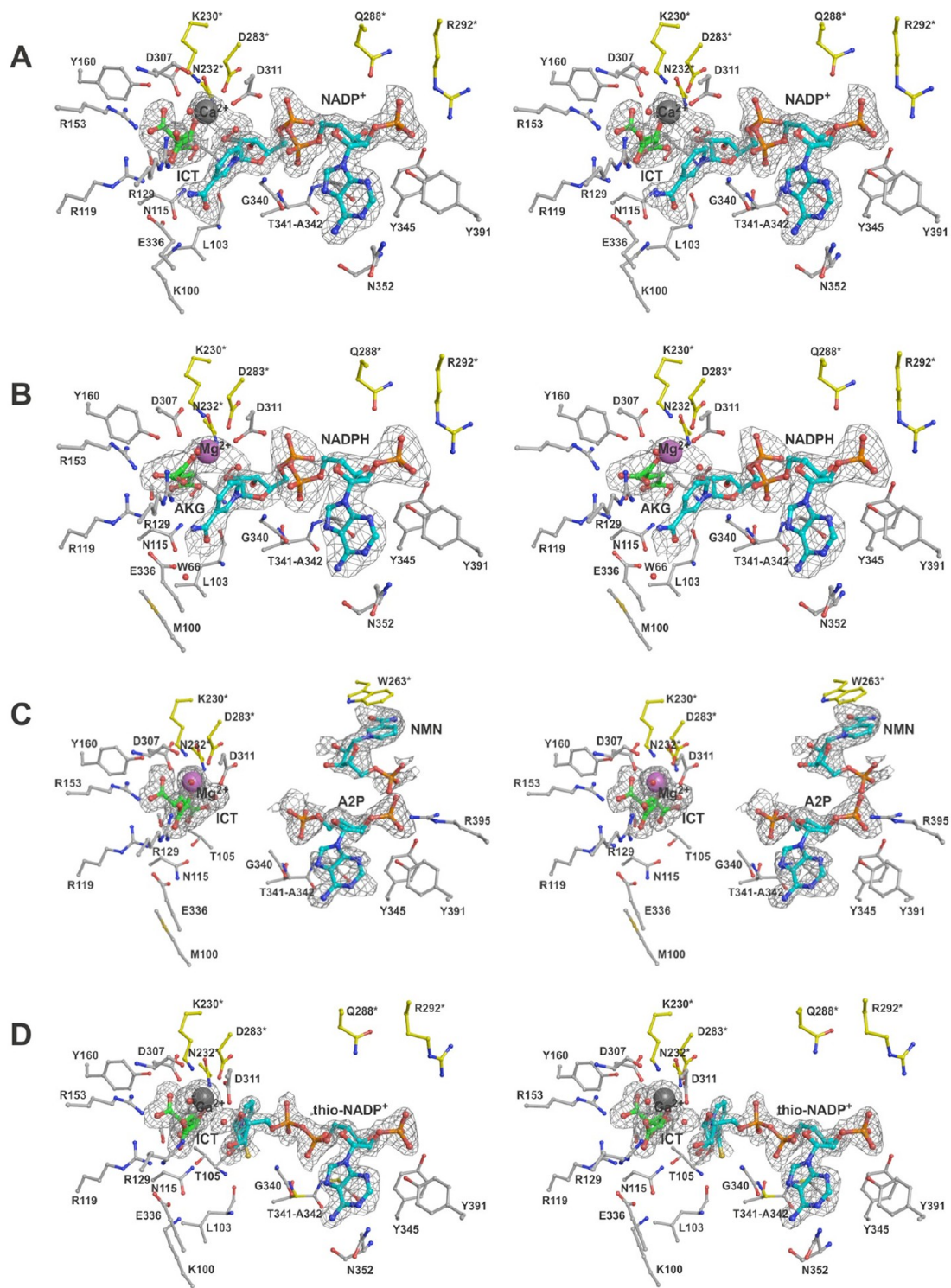
Figure 4. Stereo diagrams of ligands binding to *Eco*IDH crystal structures: (A) *wt* [Ca^{2+}:ICT:NADP$^+$], (B) K100M [Mg^{2+}:ICT:NADP$^+$] x2, (C) K100M [Mg^{2+}:ICT:NADP$^+$] x1, (D) *wt* [Ca^{2+}:ICT:thio-NADP$^+$]. Unbiased σ_A-weighted $|F_o| - |F_c|$ electron density maps covering the ligands in the catalytic pockets were obtained with PHENIX by simulated annealing in the absence of the ligands and water molecules located inside the catalytic pocket and coordinated either to Mg^{2+} or its analogue Ca^{2+}. The maps are represented as a light gray mesh and contoured at the 3σ level for all structures except for K100M [Mg^{2+}:ICT:NADP$^+$] x1 structure (C) where it is drawn at the 3σ level for the [Mg^{2+}/ICT] complex and at the 2σ level for the hydrolyzed NADP$^+$. Protein residues and polyatomic ligands are drawn as ball-and-stick, and the Mg^{2+} and Ca^{2+} metal ions and the water molecules are drawn as spheres. Atom colors are violet for magnesium, gray for calcium, orange for phosphorus, blue for nitrogen and red for oxygen; carbon atoms are colored cyan in NADP$^+$, NADPH, thio-NADP$^+$ and the hydrolysis products A2P and NMN, green in ICT and AKG, and light-gray and yellow in the protein residues from the first and second subunits of the biological homodimer respectively. For clarity, only the side-chains (starting at C$^\alpha$) of the protein residues are represented, except where the main-chain atoms interact with the ligands. Because of the orientation chosen, S113 and occasionally T105 are obscured by the ligands and not clearly visible.
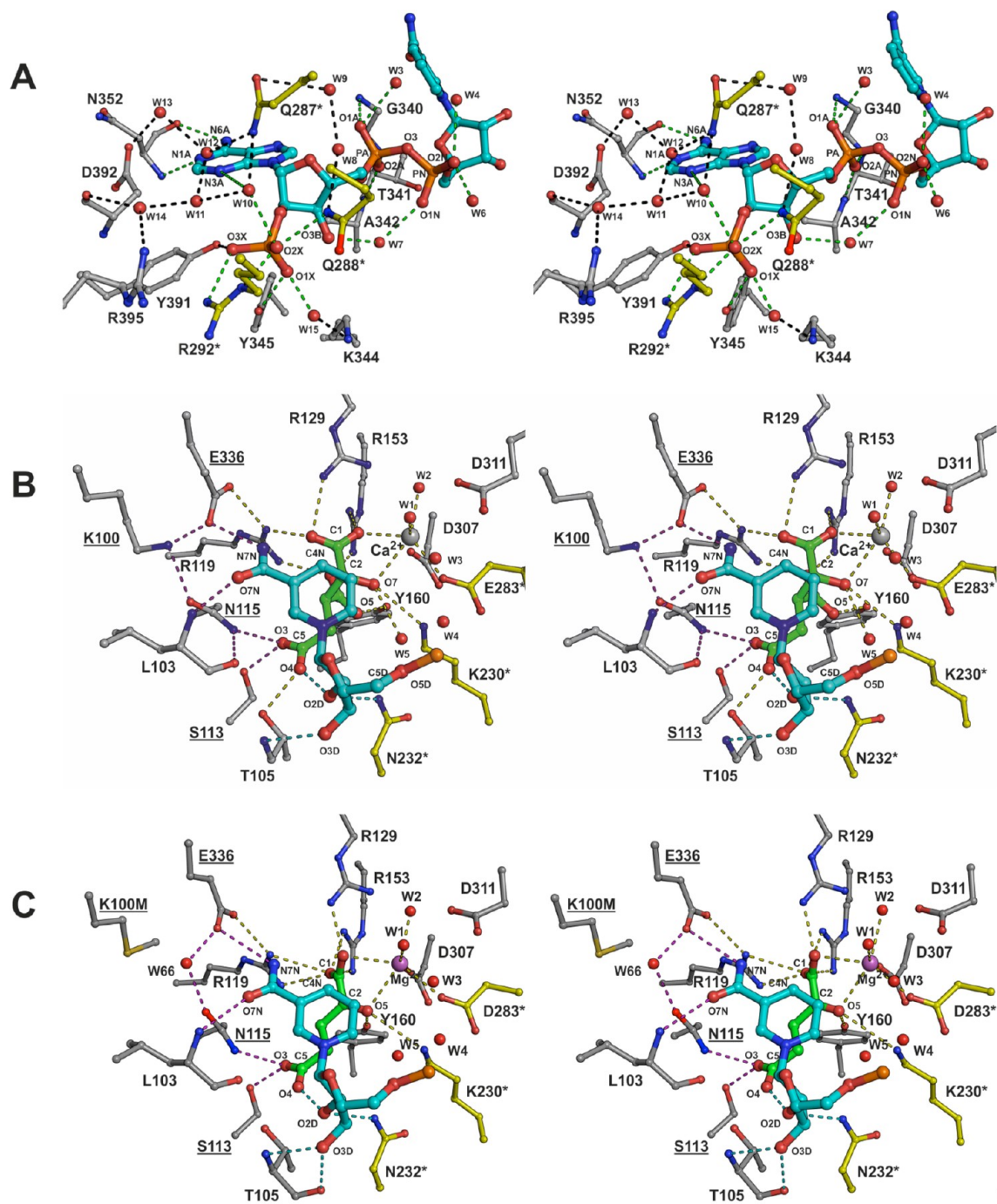
Figure 5. Stereo diagrams showing substrate and product binding in the "fully closed" *Eco*IDH crystal structures. (A) The adenosine-2′,5′-biphosphate (A2P) binding site in the *wt* [Ca^{2+}:ICT:NADP$^+$] structure. (B) the nicotinamide mononucleotide (NMN) and Ca^{2+}-isocitrate binding sites in the *wt* [Ca^{2+}:ICT:NADP$^+$] structure. (C) The nicotinamide mononucleotide (NMN) and Mg^{2+}:α-ketoglutarate binding sites in the K100M [Mg^{2+}:ICT:NADP$^+$] x2 structure. Side chains and substrates are shown as ball-and-stick with waters and Ca^{2+} shown as spheres. Dashed lines indicate hydrogen/coordination bonds and are color-coded according to the interactions made: green with A2P, cyan with the ribosyl of NMN, yellow with Ca^{2+}-isocitrate, black for interactions between side-chains and waters, and purple for interactions anchoring the nicotinamide ring and the catalytic tetrad Ser113-Asn115-Lys100-Glu336 (with residue labels underlined). Carbon atoms are colored cyan for NADP, green for isocitrate, and light gray and yellow for the first and second subunits of *Eco*IDH respectively. Residues from the second subunit are labeled with an asterisk. Ligand atoms are labeled according to Figure 1C.

Aeropyrum pernix IDH with isocitrate and NADP$^+$ (PDB 1xkd, chain B)[20] and *Acithiophilus thiooxidans* IDH with citrate and NAD$^+$ (PDB 2d4v) [56] (Figure 2E). The closure of the active site, as the large domain rotates from the "open" to the "quasi-closed" and then to the "fully closed" positions to form a

catalytically competent ternary *pseudo*-Michaelis complex, is illustrated in Figure 3.

NADP$^+$ and thio-NADP$^+$ Binding. Continuous electron densities were observed for the NADP(H) ligands in both "fully closed" *wt* [Ca^{2+}:ICT:NADP$^+$] and K100M [Mg^{2+}:ICT:NADP$^+$] x2 complexes (Figure 4A,B). Isotropic
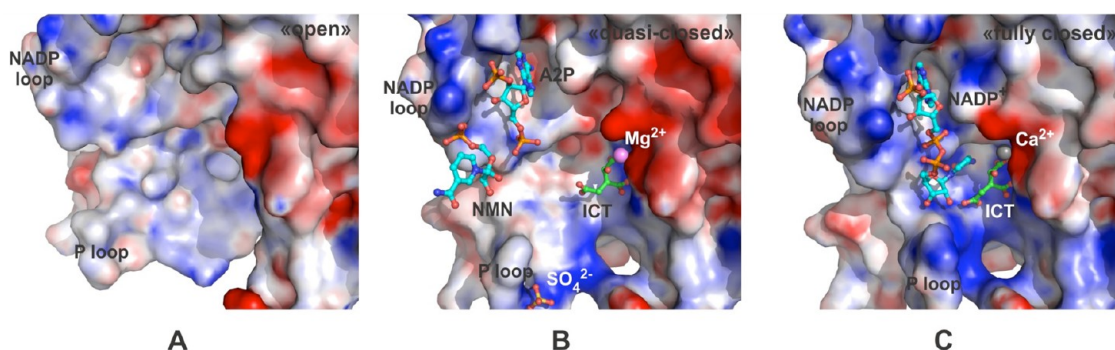
Figure 6. Changes in the electrostatic potential landscape of the *Eco*IDH active site between the "open", "quasi-closed", and "fully closed" conformations. (A) The "open" form (PDB 1sjs);[53] (B) The "quasi-closed" form, represented by the K100M [Mg^{2+}:ICT:$NADP^+$] x1 monomer; (C) The catalytically competent "fully closed" conformation, represented by the *wt* [Ca^{2+}:ICT:$NADP^+$] monomer. The electrostatic potential of each biological homodimer is represented at the molecular surface of the respective monomer (the second monomer is not shown for clarity). The atomic charges for each homodimer were calculated with PDB2PQR[62] using the CHARMM22[63] all-atom force field for the protein atoms. The electrostatic distribution was determined with the APBS v0.4.0 PyMol plug-in[64] by applying the nonlinear Poisson−Boltzmann method with $T = 300$ K, an ionic strength of 0.15 M, a solvent dielectric constant $\varepsilon_s = 80$ and a protein dielectric constant $\varepsilon_p = 6$. The molecular surface of each monomer was calculated using a solvent probe radius of 1.4 Å. The range of electrostatic potentials shown spans from −15 (red) to +15 kT/e (blue) units. Ligands are shown as ball-and-stick and the Mg^{2+} and Ca^{2+} ions are represented as spheres. Atom colors are: violet for magnesium, gray for calcium, yellow for sulfur, orange for phosphorus, blue for nitrogen, red for oxygen, green for carbon atoms in ICT, and cyan for carbon atoms in $NADP^+$, A2P, and NMN.

atomic displacement parameters of NADP(H) atoms were comparable to those of the side-chains interacting directly with the ligands. Bound NADP(H) adopts the same catalytically productive conformation in both structures (rms deviation of 0.14 Å for all ligand atoms).

Electron densities corresponding to NADP(H) in the "quasi-closed" K100M [Mg^{2+}:ICT:$NADP^+$] x1 and K100M [Ca^{2+}:α-KG:NADPH]) complexes were not continuous. In both complexes the adenosine 2′,5′-diphosphate moieties (A2P) of NADP were similarly bound in the A2P binding pocket (Figure 4C; rms deviation of 0.10 Å) and refined with partial occupancies of 0.64 and 0.67, respectively. The isotropic atomic displacement parameters for the A2P atoms increased progressively from the adenine ring toward the 5′-phosphate, whereas those of the side-chains interacting directly with A2P remained approximately constant. Fragments corresponding to the nicotinamide mononucleotide (NMN) moiety of NADP, or the corresponding mononucleoside, were identified at the end of the β-sheet in the "quasi-closed" K100M [Mg^{2+}:ICT:$NADP^+$] x1 and the " fully closed" K100M [Mg^{2+}:ICT:$NADP^+$] x2 complexes. No similar fragment could be identified in the K100M [Ca^{2+}:α-KG:NADPH] complex where only the A2P moiety was visible.

Continuous well-defined electron densities with low isotropic atomic displacement parameters were observed for the thio-$NADP^+$ analogues in the *wt* [Ca^{2+}:ICT:thio-$NADP^+$] and K100M [Mg^{2+}:ICT:thio-$NADP^+$] complexes (Figure 4D), with refined occupancies of 0.79 and 0.75, respectively. Bound thio-$NADP^+$ adopts the same catalytically unproductive conformation in both structures (rms deviation of 0.12 Å for all ligand atoms).

The Adenosine-2′,5′-biphosphate (A2P) Binding Site. The A2P binding site is defined by the interdomain 3/10 helix (residues 318−324) on one side of the adenine ring, the NADP-binding loop (residues 336−352) on the opposite side, and α-helix "l" (residues 390−397) which is oriented obliquely to the plane of the ring (Figure 1A). In all structures the adenine ring π-stacks with His339. The adenine ring and the endocyclic ribose oxygen adopt the typical *anti*-conformation

with respect to each other around the N-glycosidic bond, and the ribose ring binds in an approximate half-chair C2′-exo/C3′-endo conformation (Figure 5A).[20,27,32,57] The nitrogen atoms of the adenine ring are involved in several hydrogen bonds: N6A to the carbonyl oxygen of Asn352, N1A to the amide nitrogen of Asn352, and N3A to water W10. This water forms part of a hydrogen-bonded chain of five solvent molecules (W10−W14), present only in the "fully closed" conformation of IDH (Figure 5A), linking α-helices "i" and "h*" to α-helix "l" of the large domain. The protein atoms involved in this network are Asp392 $O^{\delta2}$, Gln287* $N^{\varepsilon2}$, Arg395 $N^{\eta2}$, and Asp392 O.

In all structures O1X and O3X of the 5′-phosphate group hydrogen bond to the side chain hydroxyls of Tyr345 and Tyr391, respectively. In the "fully closed" conformations additional hydrogen bonds form between O2X and Gln288* $N^{\varepsilon2}$ and Arg292* N^{ε}, O3X and Arg292* $N^{\eta1}$, while W15 bridges O1X to Lys344 N and W10 bridges O2X to Gln287* $O^{\varepsilon1}$ (Figure 5A). The PA center of the pyrophosphate hydrogen-bonds via O1A and O2A to the backbone amide of residues Gly340 and Ala342 in the NADP-binding loop (Figure 5A). The NADP(H) pyrophosphate backbone, which adopts a PA−O3-PN-O5D dihedral angle of 92°, contributes to the assembly of a six atom ring formed by four water molecules, the C2 hydroxyl of isocitrate and the active site Mg^{2+} or Ca^{2+}.

In the "quasi-closed" conformations the A2P binding site is displaced as a rigid-body, with interactions between the large domain and α-helix "h*" replaced by bulk solvent molecules and by Arg395 $N^{\eta1}$. The interaction with Gly340 is absent in structures with bound thio-$NADP^+$, and the pyrophosphate backbone adopts a different conformation with PA−O3-PN-O5D dihedral angles of 133° in the K100M [Mg^{2+}:ICT:thio-$NADP^+$] complex and 114° in the *wt* [Ca^{2+}:ICT:thio-$NADP^+$] complex. This places the thio-nicotinamide mononucleotide at the entrance of the isocitrate binding pocket in a conformation flipped relative to NMN in the "fully closed" structures (Figure 4D).

The Nicotinamide Mononucleotide (NMN) Binding Site. The NMN binding site lies adjacent to the isocitrate

binding pocket (Figure 5B). In both "fully closed" *wt* [Ca^{2+}:ICT:$NADP^+$] and K100M [Mg^{2+}:ICT:$NADP^+$] x2 complexes, NADP(H) binds in a bent conformation with the nicotinamide ring above the substrate binding pocket, its amide oriented toward the large domain. The ribosyl moiety is anchored to the phosphorylation loop, in a roughly half-chair C2′-exo/C3′-endo conformation, with a dihedral angle of 166° about the O5D-C5D phosphoester bond. The 3′-hydroxyl O3D hydrogen-bonds to Thr105 N and Thr105 O. The 2′-hydroxyl O2D interacts with a C5 carboxylate oxygen of isocitrate or α-ketoglutarate, as well as with Asn232* $N^{\delta 2}$. These interactions trigger a shift in the phosphorylation loop toward the active site pocket where it acts as a platform to bind NADP in a catalytically productive conformation (Figure 6).

In the *wt* [Ca^{2+}:ICT:$NADP^+$] *pseudo*-Michaelis complex, the amide N7N hydrogen bonds to the C1 carboxylate of isocitrate (3.1 Å) and Glu336 $O^{\epsilon 1}$ (2.9 Å), while the O7N hydrogen bonds with Leu103 N (2.9 Å) and Asn115 $N^{\delta 2}$ (3.0 Å) (Figure 5B). Similarly, in the K100M [Mg^{2+}:ICT:$NADP^+$] x2 ternary product complex the N7N is within van der Waals distance of the C1 carboxylate of α-ketoglutarate (3.8 Å) and hydrogen bonds to Glu336 $O^{\epsilon 1}$ (3.2 Å), while O7N hydrogen bonds with water W66 (2.9 Å, and near Lys100 N^{ς} in the *pseudo*-Michaelis complex) and Asn115 $N^{\delta 1}$ (2.9 Å) (Figure 5C). The Lys100-Leu103-Asn115-Glu336 tetrad (Figure 5B,C) plays a central role both in anchoring the nicotinamide ring and in triggering a cascade of electrostatic interactions that propagate toward the hinge region of the central β-sheet, facilitating the full closure of the enzyme. In particular, Asn115 plays a pivotal role in anchoring both the NMN moiety and isocitrate in a conformation favorable to catalysis.

In both "fully closed" complexes, the nicotinamide ring lies with its C4N poised to receive the hydride from isocitrate C2 on its *re* face (Figure 5B,C). In structures with bound thio-$NADP^+$, the entire thio-NMN moiety is rotated 166° about the O5D-C5D phosphoester bond. The C4N now points away from the active site while the *si* face of the nicotinamide ring lies against the C5 carboxylate of isocitrate. This flipped conformation is stabilized by a hydrogen bond from the N7N of the thioacetamyl to Thr105 O and interactions between the ribosyl-moiety of thio-NMN and waters that fill the NMN binding pocket.

Evidence that $NADP^+$ might be hydrolyzed in *Eco*IDH crystals was first obtained when a fragment corresponding to the missing NMN moiety was observed in the "quasi-closed" K100M [Mg^{2+}:ICT:$NADP^+$] x1 (Figure 4C) and "fully closed" the K100M [Mg^{2+}:ICT:$NADP^+$] x2 complexes. In both instances, the *si* face of the nicotinamide ring stacks against the aromatic ring of Trp263* with the carboxamide stabilized by the loop formed by residues 258−261. Preliminary evidence for hydrolytic activity by *Eco*IDH was given by mass spectrometry analysis (unpublished results). These studies detected the presence of hydrolyzed $NADP^+$ products in redissolved tetragonal crystals of both *wt*IDH and K100M IDH soaked with $NADP^+$, but not when $NADP^+$ was added to the protein solutions. Despite their qualitative nature, these results suggest that the coenzyme hydrolysis occurs only in the "fully closed" or "quasi-closed" conformation of the enzyme. Further studies are required to establish the biological relevance, if any, of coenzyme hydrolysis by IDH.

The Substrate Binding Pocket. As previously described,[13] isocitrate and α-ketoglutarate bind in a pocket located at the base of the cleft between hinge axis strands "E" and "F" and helices "i" and "h*" at the dimer interface (Figure 1A). In all structures a divalent metal ion, Mg^{2+} or Ca^{2+}, chelates a C1 carboxylate oxygen and the C2 oxygen of bound isocitrate or α-ketoglutarate (a hydroxyl and a carbonyl, respectively) (Figure 5B,C). The conserved Arg119, Arg129 and Arg153 provide a binding scaffold for the C1 carboxylate − this occurs despite the 90° rotation around the C1−C2 σ-bond caused by the change in hybridization at C2 from sp^3 in isocitrate to sp^2 in α-ketoglutarate (Figure 5B,C). A Lys230*-Tyr160 diad also participates in binding the C6 carboxylate (attached to the C3 of isocitrate) and C2 hydroxyl, respectively.[21] As with the NADP-binding pocket, the partial displacement of the large domain during hinge closure produces a positional shift in the substrate binding site, with preserved hydrogen bonds to the ligand C1 and C6 carboxylates.

Both isocitrate and α-ketoglutarate bind in "active" and "inactive" conformations, as reflected in the different C2−C3−C4−C5 dihedral angles: 139° ("active") and 63° ("inactive") for isocitrate, 172° ("active") and 75° ("inactive") for α-ketoglutarate. In the "active" conformation, observed in the "fully closed" *wt* [Ca^{2+}:ICT:$NADP^+$] *pseudo*-Michaelis complex (Figure 5B), the "fully closed" K100M [Mg^{2+}:ICT:$NADP^+$] x2 ternary product complex (Figure 5C, this enzyme is active *in crystallo*) and the "quasi-closed" *wt* [Ca^{2+}:ICT:thio-$NADP^+$] complex, the C5 carboxylate hydrogen bonds with Ser113 O^{γ}, Thr105 O^{γ}, and Asn115 $N^{\delta 1}$. In the "inactive" conformation, observed in the "quasi-closed" K100M [Mg^{2+}:ICT:$NADP^+$] x1, the K100M [Mg^{2+}:ICT:thio-$NADP^+$] and the K100M [Ca^{2+}:α-KG:NADPH] complexes, the C5 carboxylate hydrogen bonds to Ser113 O^{γ} and one or more waters.

The coordination number (CN) of Mg^{2+} changes from CN = 5 to CN = 6 as the enzyme shifts from the "quasi-closed" K100M [Mg^{2+}:ICT:$NADP^+$] x1 and K100M [Mg^{2+}:ICT:thio-$NADP^+$] to the "fully closed" K100M [Mg^{2+}:ICT:$NADP^+$] x2 position. With Ca^{2+}, CN = 7 and CN = 6 in the "quasi-closed" *wt* [Ca^{2+}:ICT:thio-$NADP^+$] and K100M [Ca^{2+}:α-KG:NADPH] complexes respectively, whereas CN = 6 in the "fully closed" *wt* [Ca^{2+}:ICT:$NADP^+$] complex. The Ca^{2+} in the *wt* [Ca^{2+}:ICT:$NADP^+$] structure lies close to the Mg^{2+} in K100M [Mg^{2+}:ICT:$NADP^+$] x2 structure, effectively mirroring the Michaelis−Menten complex (Figure 5B,C). In addition to binding the isocitrate or the α-ketoglutarate ligands, Mg^{2+} coordinates to Asp307 $O^{\delta 1}$ and two water molecules, W1 and W2, the second a part of a conserved six-atom ring. This nonlabile pentavalent coordination sphere is supplemented with a sixth ligand, Asp283* $O^{\delta 2}$, that completes the Mg^{2+} coordination sphere in the "fully closed" *wt* [Ca^{2+}:ICT:$NADP^+$] and K100M [Mg^{2+}:ICT:$NADP^+$] x2 complexes. The Ca^{2+} coordination sphere also includes a transient ligand, Asp311 $O^{\delta 2}$, coordinated to the metal ion prior to full closure of the enzyme (Figure 5B).

◼ DISCUSSION

Hinge Dynamics and Substrate-Mediated Structural Rearrangements. Metal-dependent NAD(P)-linked hydroxyacid oxidative decarboxylases undergo structural rearrangements typical of many enzymes, including rigid body motions and substrate-induced conformational changes that modulate their catalytic activities.[58] Studies of *Eco*IDH have identified basic mechanisms behind substrate-induced conformational changes.[21,23,29,53] However, crystallographic intermediate-trapping methods based on crystal soaks with substrates and substrate analogues have proved insufficient to identify all the
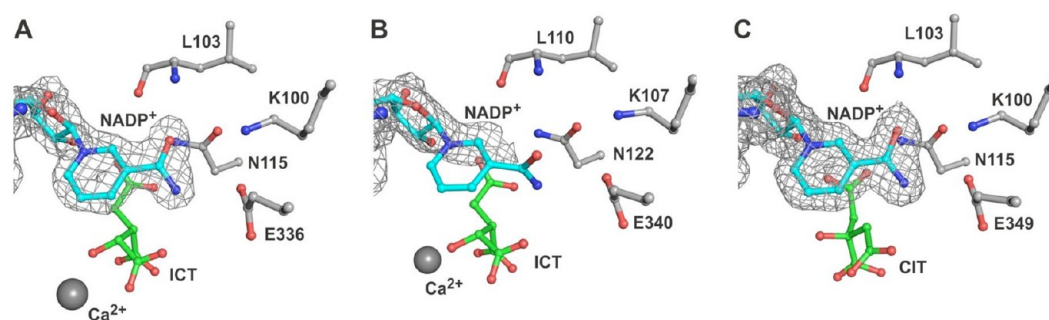
Figure 7. The nicotinamide ring of NADP$^+$ in the fully closed IDH structures: (A) *wt* [Ca^{2+}:ICT:NADP$^+$] (this work), (B) *Aeropyrum pernix* IDH (PDB 1xkd, chain B),[20] (C) *Acidithiophilus thiooxidans* IDH (PDB 2d4v, chain A).[56] σ_A-weighted 2|F_o| − |F_c| electron density maps covering NADP$^+$ were calculated with COOT using the observed and final calculated structure factors. The structure factor data for PDB 1xkd and 2d4v were downloaded from the Protein Data Bank with COOT. The maps are represented as a light gray mesh and contoured at the 1.5σ level. Protein residues and polyatomic ligands are drawn as ball-and-stick, and the Ca^{2+} metal ions are drawn as spheres. Atom colors are gray for calcium, orange for phosphorus, blue for nitrogen and red for oxygen; carbon atoms are colored cyan in NADP$^+$, green in ICT and citrate (CIT), and light-gray in the displayed protein residues. For clarity, only the side-chains (starting at C$^\alpha$) of the protein residues are represented, except where the main-chain atoms interact with the ligands.

residues involved, mostly because crystal packing is incompatible with the fast structural rearrangements taking place during catalysis.

Our cryo-trapped snapshots of the "fully closed" *wt* [Ca^{2+}:ICT:NADP$^+$] and K100M [Mg^{2+}:ICT:NADP$^+$] x2 structures provide deeper insights into the structural conformations needed to produce productive ternary complexes. Both *wt*IDH and its K100M variant undergo a more complete hinge closure than the "quasi-closed" conformations previously reported (Figure 3). In the "quasi-closed" conformation, ligands bind at the pocket surface yielding nonproductive complexes. In the "fully closed" conformation they move as rigid bodies to the inner pocket region as the large domain rotates further toward the small domain. The "fully closed" conformation is also distinguished from the "quasi-closed" conformation by two additional structural changes: a small displacement of the NADP-binding loop in the direction of the rotation (Lys 344 C$^\alpha$ moves by ca. 4 Å) and a shift in the phosphorylation loop toward the active site pocket (Gly 108 C$^\alpha$ moves by ca. 9 Å) which blocks access to bulk solvent while stabilizing the substrates in position for catalysis (Figure 6). Figure 6 also illustrates the changes in the electrostatic landscape of the catalytic pocket that result from the hinge motion upon forming a catalytically competent pseudo-Michaelis complex.

Our analysis shows that only *Acidithiophilus thiooxidans* IDH (PDB 2d4v, chains A, B, C, D)[56] and *Aeropyrum pernix* IDH (PDB 1xkd, chain B)[20] display the "fully closed" conformation of the enzyme (see Tables 4 and 5). However, the *Acidithiophilus thiooxidans* IDH structure lacks the catalytic metal ion and the ligands are an unnatural citrate and NAD$^+$. Chain B of *Aeropyrum pernix* IDH is the most similar to our *wt* [Ca^{2+}:ICT:NADP$^+$] structure, the only notable difference being that the carboxamide group was modeled perpendicular to the nicotinamide ring (C2N−C3N−C7N−O7N dihedral angle of 95.6°) rather than nearly coplanar (27.5°). Unfortunately, and in contrast with our "fully closed" structure, the electron density of the nicotinamide ring is poorly defined (Figure 7). Our *wt* [Ca^{2+}:ICT:NADP$^+$] structure is thus the first complete example of a true *pseudo*-Michaelis complex in an IDH enzyme.

Cryo-trapped product ternary complexes with bound NADPH, α-ketoglutarate and Ca^{2+} have also been reported for *Saccharomyces cerevesiae* IDH isoform 1 (*Scer*IDH1, PDB 2qfx)[30] and the R132H mutant of human IDH isoform 1

(R132H *Hsap*IDH1; PDB 3inm).[31] Despite the different electrostatic environments of their active sites, both structures share features in common with our "fully closed" *wt* [Ca^{2+}:ICT:NADP$^+$] and K100M [Mg^{2+}:ICT:NADP$^+$] x2 complexes. In all cases, Thr105 and Ser113 (*Eco*IDH numbering) are conserved in the homologous enzymes and play pivotal roles in anchoring the C5 carboxylate group of isocitrate or α-ketoglutarate and the 3′-hydroxyl group O3D of the NMN.

Together with our "fully closed" *wt* [Ca^{2+}:ICT:NADP$^+$] and K100M [Mg^{2+}:ICT:NADP$^+$] x2 complexes of *Eco*IDH, these four "fully closed" structures confirm that the significance of the structural rearrangements in the phosphorylation loop of *Eco*IDH extends beyond its role in allowing access for regulatory phosphorylation, effectively an "on-off switch",[53,55,59,60] to being directly involved in the assembly of productive ternary complexes and product release during the catalytic turnover.

The Lys100-Leu103-Asn115-Glu336 tetrad in *Eco*IDH anchors the nicotinamide ring in position for catalysis. As seen in the "fully closed" *wt* [Ca^{2+}:ICT:NADP$^+$] and K100M [Mg^{2+}:ICT:NADP$^+$] x2 complexes, Asn115 plays a central role in anchoring the C5 carboxylate of isocitrate and α-ketoglutarate, as well as helping orient the carboxamide of the nicotinamide ring (Figure 5B,C). In the "fully closed" K100M [Mg^{2+}:ICT:NADP$^+$] x2 structure, the now absent electrostatic contribution of the hydrogen bond between Lys100 and Glu336, which in turn anchors the nicotinamide ring in *wt*IDH, is rescued by a water molecule (W66) that is nearly coincident with the Lys100 N$^\zeta$ atom (Figure 5C). In fact W66 may be an NH$_4^+$ cation ((NH$_4$)$_2$SO$_4$ was the precipitant). Not only is NH$_4^+$ isoelectronic with H$_2$O, and therefore indistinguishable by X-ray crystallography at 2.7 Å resolution, but the local environment is negatively charged (provided by O7N of the NMN moiety and the carboxylate group of Glu336, and to a lesser extent by the carbonyl group of Gly101). Preliminary kinetic studies show that NH$_4^+$ partially rescues activity in the K100M mutant (unpublished observation).

The Active Site. Replacing Mg^{2+} by Ca^{2+} reduces k_{cat} > 2500-fold.[27] Theoretical studies based on small distance and angle perturbations of the C2 hydroxyl group of isocitrate and the C4N atom of the nicotinamide ring suggest that Ca^{2+} disturbs the optimal orientation (distance and angle) of the
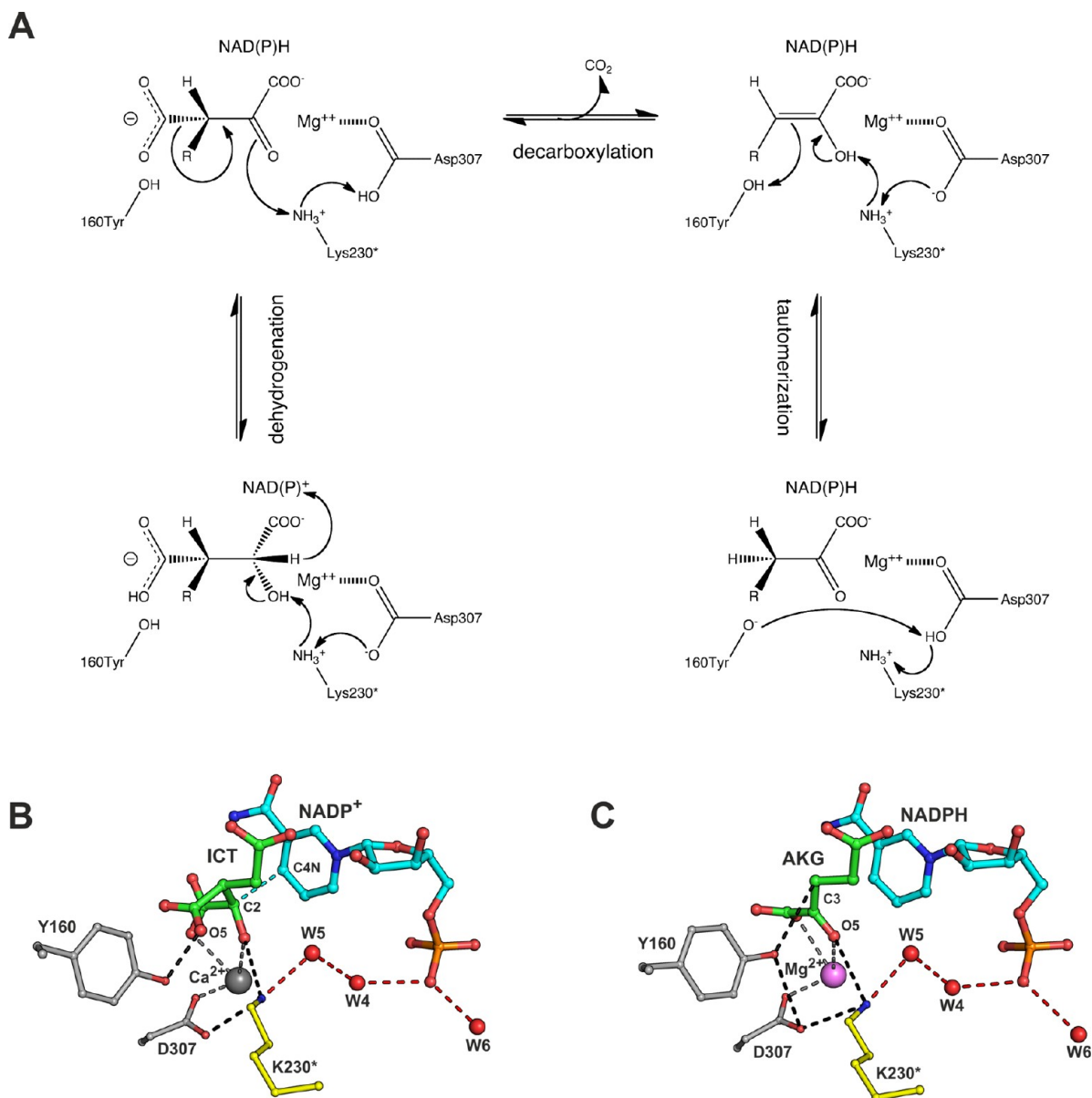
Figure 8. Structural evidence for the IDH catalytic mechanism after Aktas and Cook.[5] (A) Scheme of the catalytic mechanism of isocitrate conversion to α-ketoglutarate in IDH. (B) The *pseudo*-Michaelis complex of the *wt* [Ca^{2+}:ICT:NADP$^+$] structure mimics the dehydrogenation step, with Lys230* positioned to deprotonate the isocitrate C2 hydroxyl and the nicotinamide ring C4 poised to receive the C2 hydride. (C) Products trapped in the K100M [Mg^{2+}:ICT:NADP$^+$] ternary complex mirror the reciprocal (de)protonations by Lys230* at the C2 carbonyl and Tyr160 at C3 during the tautomerization of α-ketoglutarate following decarboxylation of the oxalosuccinate intermediate. Dashed lines indicate important interactions or hydrogen/coordination bonds and are color-coded black for the protonation/deprotonation interactions during conversion of isocitrate into α-ketoglutarate, red for a proton relay possibly involved in acid/base catalysis, and gray/violet for interactions with the Ca^{2+}/Mg^{2+} metal ion respectively. The catalytic triad residues and the ligands are shown as ball-and-stick with waters and metal ions shown as spheres. Atom colors are gray for calcium, violet for magnesium, orange for phosphorus, blue for nitrogen and red for oxygen, with carbons colored cyan for NADP$^+$/NADPH, green for isocitrate/α-ketoglutarate, and light gray and yellow for residues in the first and second subunits of *Eco*IDH, respectively.

reacting molecular orbitals for hydride transfer.[27] Yet, despite the higher ionic radius of Ca^{2+} (0.99 Å) compared to that of Mg^{2+} (0.65 Å), our results show that Ca^{2+} in the "fully closed" *wt* [Ca^{2+}:ICT:NADP$^+$] pseudo-Michaelis complex is geometrically equivalent to the Mg^{2+} metal ion observed in the "fully closed" K100M [Mg^{2+}:ICT:NADP$^+$] ternary product complex (Figure 5B,C). Being heavier than Mg^{2+}, Ca^{2+} might instead slow activity by affecting protein dynamics, perhaps by hindering mobility at the metal binding site during hinge motion. Kinetic data from *Eco*IDH,[36] pig heart IDH[12] and the related homoisocitrate dehydrogenase in yeast[10] support a

steady-state kinetic mechanism with catalysis at least 10 times faster than the structural changes needed to set up the active site for catalysis.

The *wt* [Ca^{2+}:ICT:NADP$^+$] *pseudo*-Michaelis complex and the K100M [Mg^{2+}:ICT:NADP$^+$] x2 ternary complex with bound α-ketoglutarate and NADPH portray key structural changes in the active site during catalysis (Figure 5B,C). The most significant conformational changes take place at Tyr160 and Glu336. While the change at Tyr160 arises following β-decarboxylation, that at Glu336 likely results from substituting

the amine group of Lys100 by a water molecule or a NH_4^+ cation (W66).

Catalytic Mechanism. Our structural data support, in detail, the catalytic mechanism proposed by Aktas and Cook (Figure 8A).[5] Kinetic studies of the related homoisocitrate dehydrogenase (HIDH)[61] suggest that an invariant Lys (Lys230* in EcoIDH) initiates dehydrogenation by abstracting the proton from the hydroxyl of isocitrate. Consistent with this proposal, and seen for the first time, Lys230* forms a hydrogen bond (3.2 Å) with the substrate hydroxyl in the fully "closed" wt [Ca^{2+}:ICT:NADP$^+$] pseudo-Michaelis complex (Figure 8B). Lys230* must be uncharged in order to act as a base. As predicted[5] Asp307, a metal ligand, aids proton abstraction from the hydroxyl by hydrogen bonding to Lys230*. Conversion of isocitrate into oxalosuccinate is fast[36] and, except for the observed ∼90° rotation of the C1 carboxylate upon the change in hybridization at C2 from sp^3 to sp^2, is accompanied only by minimal structural rearrangements in the active site pocket.

Next, decarboxylation of oxalosuccinate produces an enol intermediate (Figure 8A), with the C2 carbonyl reprotonated by Lys230*. Tautomerization follows loss of CO_2. An invariant Tyr (Tyr160 in EcoIDH) approaches C3 for stereospecific protonation, while Lys230* once again abstracts the proton from the C2 hydroxyl to yield the α-ketoglutarate product. In the K100M [Mg^{2+}:ICT:NADP$^+$] x2 ternary product complex, Lys230* hydrogen bonds to the C2 carbonyl while Tyr160 seems poised to (de)protonate C3, albeit 3.4 Å away (Figure 8C). Indeed, the near planar α-ketoglutarate suggests some double-bond character between C2 and C3 (reducing the C1−C2−C3-C4 dihedral angle from 20° to 0° does not greatly compromise the observed electron density). Although NMR studies detected the signature of α-hydroxyglutarate bound to pig heart IDH,[11] we detected no activity toward this substrate by E. coli wildtype and the K100M mutant enzymes (unpublished observations). Thus, the observed electron density is probably an average dominated by the carbonyl form of α-ketoglutarate with lesser contributions from the enol form.

Aktas and Cook[5] proposed that the IDH mechanism is similar to that of the malic enzyme, i.e., malate dehydrogenase (decarboxylating). In the malic enzyme a hydrogen bond exists between the catalytic Lys and Tyr, allowing dehydrogenation and decarboxylation to proceed without the need to exchange protons with other groups or with bulk solvent. Neither in the wt [Ca^{2+}:ICT:NADP$^+$] pseudo-Michaelis complex nor in the K100M [Mg^{2+}:ICT:NADP$^+$] x2 ternary product complex is there evidence of a hydrogen bond between Lys230* and Tyr160, even though their functional groups lie in close proximity. However, both are close to Asp307 in the wt [Ca^{2+}:ICT:NADP$^+$] pseudo-Michaelis complex. If a proton is not exchanged directly between Lys230* and Tyr160 during enol conversion to α-ketoglutarate, then the exchange may be indirect via Asp307 (Figure 8A). Alternatively, extending from the Lys230*-Tyr160-Asp307 catalytic triad there is a proton relay comprising two water molecules (W5 and W4), the O2N oxygen from the NADP pyrophosphate backbone and a third water molecule (W6) that may balance proton flow between the active site and the bulk solvent during catalysis (Figure 8B,C). Although a proton relay of this kind has been proposed for the pseudo-Michaelis complex of Aeropyrum pernix IDH,[20] our results provide new insights into the role played by the Lys230*-Asp307-Tyr160 catalytic triad during oxidative decarboxylation.

■ ASSOCIATED CONTENT

Ⓢ Supporting Information

Composition of the soaking solutions, the duration of each soak and the final ligand concentrations for each data set (Table S1) and a ribbon diagram of the biological homodimer in the [Ca^{2+}:ICT:NADP$^+$] crystal structure (Figure S1). This material is available free of charge via the Internet at http://pubs.acs.org.

Accession Codes

Coordinates and structure factors were deposited in the Protein Data Bank in Europe (PDBe, http://www.pdbe.org). The accession codes for the coordinate entries and the respective structure factors are 4aj3 and r4aj3sf for wt [Ca^{2+}:ICT:NADP], 4ajs and r4ajssf for K100M [Mg^{2+}:ICT:NADP$^+$] x1, 4ajr and r4ajrsf for K100M [Mg^{2+}:ICT:NADP$^+$] x2, 4ajc and r4ajcsf for K100M [Ca^{2+}:α-KG:NADPH], 4ajb and r4ajbsf for K100M [Mg^{2+}:ICT:thio-NADP$^+$], 4aja and r4ajasf for wt [Ca^{2+}:ICT:thio-NADP$^+$].

■ AUTHOR INFORMATION

Corresponding Author

*(A.M.D.) Tel: +1 612-624-7299; fax: +1 612-625-5780; e-mail: deanx024@umn.edu. (P.M.M.) Tel: +351 21 4469669; fax: +351 21 4433644; e-mail: matias@itqb.unl.pt.

Notes

The authors declare no competing financial interest.

■ ABBREVIATIONS USED

NADP$^+$, β-nicotinamide adenine dinucleotide phosphate; NADPH, β-nicotinamide adenine dinucleotide phosphate (reduced); thio-NADP$^+$, β-thio-nicotinamide adenine dinucleotide phosphate; ICT, 2R,3S-isocitrate; OXA, oxalosuccinate; α-KG or AKG, α-ketoglutarate; NMN, nicotinamide mononucleotide; thio-NMN, thionicotinamide mononucleotide; A2P, Adenosine 2′,5′-diphosphate; IPM, isopropylmalate; IDH, isocitrate dehydrogenase; EcoIDH, Escherichia coli K21 IDH; wtIDH, Escherichia coli K21 IDH (wild type); IDH (K100M), Escherichia coli K21 IDH K100M mutant; AperIDH, Aeropyrum pernix IDH; BsubIDH, Bacillus subtilis IDH; R132H HsapIDH1, R132H mutant of human IDH isoform 1; SscrIDH, Sus scrofa (porcine) IDH; ScerIDH1, Saccharomyces cerevesiae IDH (mitochondrial NADP-dependent); rms., root-mean-square

■ REFERENCES

(1) Dean, A. M., and Golding, G. B. (1997) Protein engineering reveals ancient adaptive replacements in isocitrate dehydrogenase. Proc. Natl. Acad. Sci. U. S. A. 94, 3104−3109.

(2) Garrad, R. C., and Bhattacharjee, J. K. (1992) Lysine biosynthesis in selected pathogenic fungi: characterization of lysine auxotrophs and the cloned LYS1 gene of *Candida albicans*. *J. Bacteriol. 174*, 7379–7384.

(3) Tipton, P. A., and Beecher, B. S. (1994) Tartrate dehydrogenase, a new member of the family of metal-dependent decarboxylating R-hydroxyacid dehydrogenases. *Arch. Biochem. Biophys. 313*, 15–21.

(4) Salomone, J. Y., Crouzet, P., De Ruffray, P., and Otten, L. (1996) Characterization and distribution of tartrate utilization genes in the grapevine pathogen Agrobacterium vitis. *Mol. Plant-Microbe Interact. 9*, 401–408.

(5) Aktas, D. F., and Cook, P. F. (2009) A lysine-tyrosine pair carries out acid-base chemistry in the metal ion-dependent pyridine dinucleotide-linked beta-hydroxyacid oxidative decarboxylases. *Biochemistry 48*, 3565–3577.

(6) Steinberger, R., and Westheimer, F. H. (1951) Metal ion-catalyzed decarboxylation: A model for an enzyme system. *J. Am. Chem. Soc. 73*, 429–435.

(7) Lienhard, G. E., and Rose, I. A. (1964) The mechanism of action of 6-phosphogluconate dehydrogenase. *Biochemistry 3*, 190–195.

(8) Dalziel, K., and Londesborough, J. C. (1968) The mechanisms of reductive carboxylation reactions. Carbon dioxide or bicarbonate as substrate of nicotinamide-adenine dinucleotide phosphate-linked isocitrate dehydrogenase and malic enzyme. *Biochem. J. 110*, 223–230.

(9) Siebert, G., Carsiotis, M., and Plaut, G. W. (1957) The enzymatic properties of isocitric dehydrogenase. *J. Biol. Chem. 226*, 977–991.

(10) Cook, P. F., and Cleland, W. W. (1981) pH variation of isotope effects in enzyme-catalyzed reactions. 2. Isotope-dependent step not pH dependent. Kinetic mechanism of alcohol dehydrogenase. *Biochemistry 20*, 1805–1816.

(11) Ehrlich, R. S., and Colman, R. F. (1987) Ionization of isocitrate bound to pig heart NADP$^+$-dependent isocitrate dehydrogenase: ^{13}C NMR study of substrate binding. *Biochemistry 26*, 3461–3466.

(12) Grissom, C. B., and Cleland, W. W. (1988) Isotope effect studies of the chemical mechanism of pig heart NADP isocitrate dehydrogenase. *Biochemistry 27*, 2934–2943.

(13) Hurley, J. H., Dean, A. M., Koshland, D. E., Jr., and Stroud, R. M. (1991) Catalytic mechanism of NADP(+)-dependent isocitrate dehydrogenase: implications from the structures of magnesium-isocitrate and NADP$^+$ complexes. *Biochemistry 30*, 8671–8678.

(14) Stoddard, B. L., Dean, A., and Bash, P. A. (1996) Combining Laue diffraction and molecular dynamics to study enzyme intermediates. *Nat. Struct. Biol. 3*, 590–595.

(15) Stoddard, B. L., Dean, A., and Koshland, D. E., Jr. (1993) Structure of isocitrate dehydrogenase with isocitrate, nicotinamide adenine dinucleotide phosphate, and calcium at 2.5-Å resolution: a *pseudo-Michaelis* ternary complex. *Biochemistry 32*, 9310–9316.

(16) Brubaker, M. J., Dyer, D. H., Stoddard, B., and Koshland, D. E., Jr. (1996) Synthesis, kinetics, and structural studies of a photolabile caged isocitrate: a catalytic trigger for isocitrate dehydrogenase. *Biochemistry 35*, 2854–2864.

(17) Grodsky, N. B., Soundar, S., and Colman, R. F. (2000) Evaluation by site-directed mutagenesis of aspartic acid residues in the metal site of pig heart NADP-dependent isocitrate dehydrogenase. *Biochemistry 39*, 2193–2200.

(18) Huang, Y. C., Grodsky, N. B., Kim, T.-K., and Colman, R. F. (2004) Ligands of the Mn^{2+} bound to porcine mitochondrial NADP-dependent isocitrate dehydrogenase, as assessed by mutagenesis. *Biochemistry 43*, 2821–2828.

(19) Ceccarelli, C., Grodsky, N. B., Ariyaratne, N., Colman, R. F., and Bahnson, B. J. (2002) Crystal structure of porcine mitochondrial NADP$^+$-dependent isocitrate dehydrogenase complexed with Mn^{2+} and isocitrate. Insights into the enzyme mechanism. *J. Biol. Chem. 277*, 43454–43462.

(20) Karlstrom, M., Stokke, R., Steen, I. H., Birkeland, N. K., and Ladenstein, R. (2005) Isocitrate dehydrogenase from the hyperthermophile *Aeropyrum pernix*: X-ray structure analysis of a ternary enzyme-substrate complex and thermal stability. *J. Mol. Biol. 345*, 559–577.

(21) Lee, M. E., Dyer, D. H., Klein, O. D., Bolduc, J. M., Stoddard, B. L., and Koshland, D. E., Jr. (1995) Mutational analysis of the catalytic residues lysine 230 and tyrosine 160 in the NADP$^+$-dependent isocitrate dehydrogenase from *Escherichia coli*. *Biochemistry 34*, 378–384.

(22) Hurley, J. H., Dean, A. M., Sohl, J. L., Koshland, D. E., Jr., and Stroud, R. M. (1990) Regulation of an enzyme by phosphorylation at the active site. *Science 249*, 1012–1016.

(23) Bolduc, J. M., Dyer, D. H., Scott, W. G., Singer, P., Sweet, R. M., Koshland, D. E., Jr., and Stoddard, B. L. (1995) Mutagenesis and Laue structures of enzyme intermediates: isocitrate dehydrogenase. *Science 268*, 1312–1318.

(24) Chen, R., Dean, A. M., Grobler, J. A., and Hurley, J. H. (1996) Second-site suppression of regulatory phosphorylation in Escherichia coli isocitrate dehydrogenase. *Protein Sci. 5*, 287–295.

(25) Cherbavaz, D. B., Lee, M. E., Stroud, R. M., and Koshland, D. E., Jr. (2000) Active site water molecules revealed in the 2.1 Å resolution structure of a site-directed mutant of isocitrate dehydrogenase. *J. Mol. Biol. 295*, 377–385.

(26) Imada, K., Inagaki, K., Matsunami, H., Kawaguchi, H., Tanaka, H., Tanaka, N., and Namba, K. (1998) Structure of 3-isopropylmalate dehydrogenase in complex with 3-isopropylmalate at 2.0 Å resolution: the role of Glu88 in the unique substrate-recognition mechanism. *Structure 6*, 971–982.

(27) Mesecar, A. D., Stoddard, B. L., and Koshland, D. E., Jr. (1997) Orbital steering in the catalytic power of enzymes: small structural changes with large catalytic consequences. *Science 277*, 202–206.

(28) Stoddard, B. L., Cohen, B. E., Brubaker, M., Mesecar, A. D., and Koshland, D. E., Jr. (1998) Millisecond Laue structures of an enzyme-product complex using photocaged substrate analogs. *Nat. Struct. Biol. 5*, 891–897.

(29) Doyle, S. A., Beernink, P. T., and Koshland, D. E., Jr. (2001) Structural basis for a change in substrate specificity: crystal structure of S113E isocitrate dehydrogenase in a complex with isopropylmalate, Mg^{2+}, and NADP. *Biochemistry 40*, 4234–4241.

(30) Peng, Y., Zhong, C., Huang, W., and Ding, J. (2008) Structural studies of *Saccharomyces cerevesiae* mitochondrial NADP-dependent isocitrate dehydrogenase in different enzymatic states reveal substantial conformational changes during the catalytic reaction. *Protein Sci. 17*, 1542–1554.

(31) Dang, L., White, D. W., Gross, S., Bennett, B. D., Bittinger, M. A., Driggers, E. M., Fantin, V. R., Jang, H. G., Jin, S., Keenan, M. C., Marks, K. M., Prins, R. M., Ward, P. S., Yen, K. E., Liau, L. M., Rabinowitz, J. D., Cantley, L. C., Thompson, C. B., Vander Heiden, M. G., and Su, S. M. (2009) Cancer-associated IDH1 mutations produce 2-hydroxyglutarate. *Nature 462*, 739–744.

(32) Yang, B., Zhong, C., Peng, Y., Lai, Z., and Ding, J. (2010) Molecular mechanisms of "off-on switch" of activities of human IDH1 by tumor-associated mutation R132H. *Cell Res. 20*, 1188–1200.

(33) Malik, R., and Viola, R. E. (2010) Structural characterization of tartrate dehydrogenase: a versatile enzyme catalyzing multiple reactions. *Acta Crystallogr. D 66*, 673–684.

(34) Kim, T.-K., Lee, P., and Colman, R. F. (2003) Critical role of Lys212 and Tyr140 in porcine NADP-dependent isocitrate dehydrogenase. *J. Biol. Chem. 278*, 49323–49331.

(35) Miller, S. P., Lunzer, M., and Dean, A. M. (2006) Direct demonstration of an adaptive constraint. *Science 314*, 458–461.

(36) Dean, A. M., and Koshland, D. E., Jr. (1993) Kinetic mechanism of *Escherichia coli* isocitrate dehydrogenase. *Biochemistry 32*, 9302–9309.

(37) Bradford, M. M. (1976) A rapid and sensitive method for the quantitation of microgram quantities of protein utilizing the principle of protein-dye binding. *Anal. Biochem. 72*, 248–254.

(38) Hurley, J. H., Thorsness, P. E., Ramalingam, V., Helmers, N. H., Koshland, D. E., Jr., and Stroud, R. M. (1989) Structure of a bacterial enzyme regulated by phosphorylation, isocitrate dehydrogenase. *Proc. Natl. Acad. Sci. U. S. A. 86*, 8635–8639.

(39) Kabsch, W. (1993) Automatic processing of rotation diffraction data from crystals of initially unknown symmetry and cell constants. *J. Appl. Crystallogr. 26*, 795−800.

(40) Winn, M. D., Ballard, C. C., Cowtan, K. D., Dodson, E. J., Emsley, P., Evans, P. R., Keegan, R. M., Krissinel, E. B., Leslie, A. G. W., McCoy, A., McNicholas, S. J., Murshudov, G. N., Pannu, N. S., Potterton, E. A., Powell, H. R., Read, R. J., Vagin, A., and Wilson, K. S. (2011) Overview of the CCP4 suite and current developments. *Acta Crystallogr. D 67*, 235−242.

(41) Storoni, L. C., McCoy, A. J., and Read, R. J. (2004) Likelihood-enhanced fast rotation functions. *Acta Crystallogr. D 60*, 432−438.

(42) Matthews, B. W. (1968) Solvent content of protein crystals. *J. Mol. Biol. 33*, 491−497.

(43) Adams, P. D., Afonine, P. V., Bunkoczi, G., Chen, V. B., Davis, I. W., Echols, N., Headd, J. J., Hung, L. W., Kapral, G. J., Grosse-Kunstleve, R. W., McCoy, A. J., Moriarty, N. W., Oeffner, R., Read, R. J., Richardson, D. C., Richardson, J. S., Terwilliger, T. C., and Zwart, P. H. (2010) PHENIX: a comprehensive Python-based system for macromolecular structure solution. *Acta Crystallogr. D 66*, 213−221.

(44) Vagin, A. A., Murshudov, G. N., and Strokopytov, B. V. (1998) BLANC: the program suite for protein crystallography. *J. Appl. Crystallogr. 31*, 98−102.

(45) Emsley, P., Lohkamp, B., Scott, W. G., and Cowtan, K. (2010) Features and development of Coot. *Acta Crystallogr. D 66*, 486−501.

(46) Lebedev, A. A., Young, P., Isupov, M. N., Moroz, O. V., Vagin, A. A., and Murshudov, G. N. (2012) JLigand: a graphical tool for the CCP4 template-restraint library. *Acta Crystallogr. D 68*, 431−440.

(47) Perrakis, A., Harkiolaki, M., Wilson, K. S., and Lamzin, V. S. (2001) ARP/wARP and molecular replacement. *Acta Crystallogr. D 57*, 1445−1450.

(48) Chen, V. B., Arendall, W. B., III, Headd, J. J., Keedy, D. A., Immormino, R. M., Kapral, G. J., Murray, L. W., Richardson, J. S., and Richardson, D. C. (2010) MolProbity: all-atom structure validation for macromolecular crystallography. *Acta Crystallogr. D 66*, 12−21.

(49) Velankar, S., Best, C., Beuth, B., Boutselakis, C. H., Cobley, N., Sousa Da Silva, A. W., Dimitropoulos, D., Golovin, A., Hirshberg, M., John, M., Krissinel, E. B., Newman, R., Oldfield, T., Pajon, A., Penkett, C. J., Pineda-Castillo, J., Sahni, G., Sen, S., Slowley, R., Suarez-Uruena, A., Swaminathan, J., van Ginkel, G., Vranken, W. F., Henrick, K., and Kleywegt, G. J. (2010) PDBe: Protein Data Bank in Europe. *Nucleic Acids Res. 38*, D308−D317.

(50) Kabsch, W. (1976) Solution for best rotation to relate 2 sets of vectors. *Acta Crystallogr. A 32*, 922−923.

(51) Hayward, S., and Berendsen, H. J. (1998) Systematic analysis of domain motions in proteins from conformational change: new results on citrate synthase and T4 lysozyme. *Proteins 30*, 144−154.

(52) Potterton, E., Briggs, P., Turkenburg, M., and Dodson, E. (2003) A graphical user interface to the CCP4 program suite. *Acta Crystallogr. D 59*, 1131−1137.

(53) Finer-Moore, J., Tsutakawa, S. E., Cherbavaz, D. B., LaPorte, D. C., Koshland, D. E., and Stroud, R. M. (1997) Access to phosphorylation in isocitrate dehydrogenase may occur by domain shifting. *Biochemistry 36*, 13890−13896.

(54) Krissinel, E., and Henrick, K. (2004) Secondary-structure matching (SSM), a new tool for fast protein alignment in three dimensions. *Acta Crystallogr. D 60*, 2256−2268.

(55) Zheng, J., and Jia, Z. (2010) Structure of the bifunctional isocitrate dehydrogenase kinase/phosphatase. *Nature 465*, 961−965.

(56) Imada, K., Tamura, T., Takenaka, R., Kobayashi, I., Namba, K., and Inagaki, K. (2008) Structure and quantum chemical analysis of NAD+-dependent isocitrate dehydrogenase: hydride transfer and co-factor specificity. *Proteins 70*, 63−71.

(57) Sidhu, N. S., Delbaere, L. T., and Sheldrick, G. M. (2011) Structure of a highly NADP(+)-specific isocitrate dehydrogenase. *Acta Crystallogr. D 67*, 856−869.

(58) Hurley, J. H., and Dean, A. M. (1994) Structure of 3-isopropylmalate dehydrogenase in complex with NAD+: ligand-induced loop closing and mechanism for cofactor specificity. *Structure 2*, 1007−1016.

(59) Xu, X., Zhao, J., Xu, Z., Peng, B., Huang, Q., Arnold, E., and Ding, J. (2004) Structures of human cytosolic NADP-dependent isocitrate dehydrogenase reveal a novel self-regulatory mechanism of activity. *J. Biol. Chem. 279*, 33946−33957.

(60) Cozzone, A. J., and El-Mansi, M. (2005) Control of isocitrate dehydrogenase catalytic activity by protein phosphorylation in *Escherichia coli*. *J. Mol. Microbiol. Biotechnol. 9*, 132−146.

(61) Lin, Y., West, A. H., and Cook, P. F. (2009) Site-directed mutagenesis as a probe of the acid-base catalytic mechanism of homoisocitrate dehydrogenase from *Saccharomyces cerevisiae*. *Biochemistry 48*, 7305−7312.

(62) Dolinsky, T. J., Nielsen, J. E., McCammon, J. A., and Baker, N. A. (2004) PDB2PQR: an automated pipeline for the setup of Poisson-Boltzmann electrostatics calculations. *Nucleic Acids Res. 32*, W665−667.

(63) MacKerell, A. D., Bashford, D., Bellott, Dunbrack, R. L., Evanseck, J. D., Field, M. J., Fischer, S., Gao, J., Guo, H., Ha, S., Joseph-McCarthy, D., Kuchnir, L., Kuczera, K., Lau, F. T. K., Mattos, C., Michnick, S., Ngo, T., Nguyen, D. T., Prodhom, B., Reiher, W. E., Roux, B., Schlenkrich, M., Smith, J. C., Stote, R., Straub, J., Watanabe, M., Wiorkiewicz-Kuczera, J., Yin, D., and Karplus, M. (1998) All-atom empirical potential for molecular modeling and dynamics studies of proteins. *J. Phys. Chem. B 102*, 3586−3616.

(64) Baker, N. A., Sept, D., Joseph, S., Holst, M. J., and McCammon, J. A. (2001) Electrostatics of nanosystems: Application to micro-tubules and the ribosome. *Proc. Natl. Acad. Sci. U. S. A. 98*, 10037−10041.

(65) Diederichs, K., and Karplus, P. A. (1997) Improved R-factors for diffraction data analysis in macromolecular crystallography. *Nat. Struct. Biol. 4*, 269−275.

(66) Hurley, J. H., Dean, A. M., Thorsness, P. E., Koshland, D. E., Jr., and Stroud, R. M. (1990) Regulation of isocitrate dehydrogenase by phosphorylation involves no long-range conformational change in the free enzyme. *J. Biol. Chem. 265*, 3599−3602.

(67) Stoddard, B. L., and Koshland, D. E., Jr. (1993) Structure of isocitrate dehydrogenase with alpha-ketoglutarate at 2.7-Å resolution: conformational changes induced by decarboxylation of isocitrate. *Biochemistry 32*, 9317−9322.

(68) Hurley, J. H., Chen, R., and Dean, A. M. (1996) Determinants of cofactor specificity in isocitrate dehydrogenase: structure of an engineered NADP+ → NAD+ specificity-reversal mutant. *Biochemistry 35*, 5670−5678.

(69) Mesecar, A. D., and Koshland, D. E., Jr. (2000) A new model for protein stereospecificity. *Nature 403*, 614−615.

(70) Mesecar, A. D., and Koshland, D. E. (2000) Sites of binding and orientation in a four-location model for protein stereospecificity. *IUBMB Life 49*, 457−466.

(71) Yates, S. P., Edwards, T. E., Bryan, C. M., Stein, A. J., Van Voorhis, W. C., Myler, P. J., Stewart, L. J., Zheng, J., and Jia, Z. (2011) Structural basis of the substrate specificity of bifunctional isocitrate dehydrogenase kinase/phosphatase. *Biochemistry 50*, 8103−8106.

(72) Singh, S. K., Matsuno, K., LaPorte, D. C., and Banaszak, L. J. (2001) Crystal structure of *Bacillus subtilis* isocitrate dehydrogenase at 1.55 Å. Insights into the nature of substrate specificity exhibited by *Escherichia coli* isocitrate dehydrogenase kinase/phosphatase. *J. Biol. Chem. 276*, 26154−26163.